Future magnitude 7.5 earthquake offshore Martinique: spotlight on the main source features controlling ground motion prediction

Elif Oral, Claudio Satriano

Geophysical Journal International

Geophys. J. Int. (2021) **227,** 1076–1093
Advance Access publication 2021 June 25
GJI Seismology

https://doi.org/10.1093/gji/ggab245

Future magnitude 7.5 earthquake offshore Martinique: spotlight on the main source features controlling ground motion prediction

Elif Oral [1,2] and Claudio Satriano [1]

[1] *Université de Paris, Institut de physique du globe de Paris, CNRS, F-*75005 *Paris, France. E-mail: elifo@caltech.edu*
[2] *Université Côte d'Azur, IRD, CNRS, Observatoire de la Côte d'Azur, Géoazur,* 06560 *Valbonne, France*

Accepted 2021 June 15. Received 2021 June 7; in original form 2020 October 27

SUMMARY

The eastern offshore of Martinique is one of the active areas of the Lesser Antilles Subduction Zone (LASZ). Although its seismicity is moderate compared to other subduction zones, LASZ is capable of generating a M 7+ interplate earthquake and recent studies and historical events, such as the M 8 1839 and M 7–7.5 1946 earthquakes, confirm this possibility. Given the high risk that Martinique can face in case of unpreparedness for such a M 7+ earthquake, and the lack of a regional seismic hazard study, we investigated through numerical modelling how ground motion can vary for a hypothetical M_w 7.5 interplate earthquake. Our main objective is to highlight the major factors related to earthquake source that can cause the highest variation in ground motion at four broad-band seismic stations across Martinique. For this purpose, we generated 320 rupture scenarios through a fractal kinematic source model, by varying rupture directivity, source dimension, slip distribution. We computed the broad-band ground motion (0.5–25 Hz) by convolution of source–time functions with empirical Green's functions (EGFs), that we selected from the analysis of moderate events (M 4–4.5) recorded in the area of interest since 2016 by the West Indies network. We found that the fault geometry and the spatial extension of the largest slip patch are the most influential factors on ground motion. The significance of the variation of the predicted ground motion with respect to ground motion prediction equations (GMPEs) depends on the evaluated frequency of ground motion and on the station. Moreover, we concluded that the EGF selection can be another significant factor controlling the modelled ground motion depending on station. Our results provide a new insight for the seismic source impact on ground motion across Martinique and can guide future blind seismic hazard assessment studies in different regions.

Key words: North America; Computational seismology; Earthquake ground motions; Earthquake source observations; Dynamics and mechanics of faulting.

1 INTRODUCTION

Martinique is located on the Lesser Antilles Subduction Zone (LASZ, Fig. 1), that is moderately active but capable of generating a M 7+ interplate earthquake (e.g. Feuillet *et al.* 2011). LASZ is formed by the subduction of the Atlantic oceanic lithosphere under the Caribbean Plate at a relatively slow convergence rate of 18 mm yr^{-1} (DeMets *et al.* 2010). Martinique island is part of the north–south trending magmatic arc of LASZ. The seismicity of LASZ can be divided into: (1) flat-thrust interplate events above approximately 50 km in the forearc; (2) deep intraslab events in the backarc; (3) intraplate events within the Carribean Plate (Russo *et al.* 1992; Laigle *et al.* 2013; Ruiz *et al.* 2013). The scarcity of large ($M > 7$) interplate thrust earthquakes in LASZ implies an unusual strain release compared to other subduction zones (Russo *et al.* 1992). Nonetheless, past studies (Ruiz *et al.* 2013; Laigle *et al.* 2013; Weil-Accardo *et al.* 2016) proposed that LASZ has high potential to generate a megathrust earthquake: the seismogenic zone might extend to the mantle wedge, below the forearc, and moderate seismic activity at the base of the seismogenic zone can load shallower segments and initiate a larger mega-thrust event. A similar mechanism has been proposed for the Japan trench subduction zone, leading to the 2011 M_w 9 Tohoku earthquake (Satriano *et al.* 2014; Barbot 2020). Laigle *et al.* (2013) and Satriano *et al.* (2014) point to the similarities between Japan trench and LASZ—such as the lack of tremors and very-slow-low-frequency earthquakes, and the sustained activity in the mantle wedge—to better understand the long-term seismic activity of LASZ. Indeed, the recent study of Paulatto *et al.* (2017), linking heterogeneity of V_p/V_s ratio to earthquake activity in LASZ, supports the proposed tectonic explanation and the analogy between Japan Trench and LASZ.

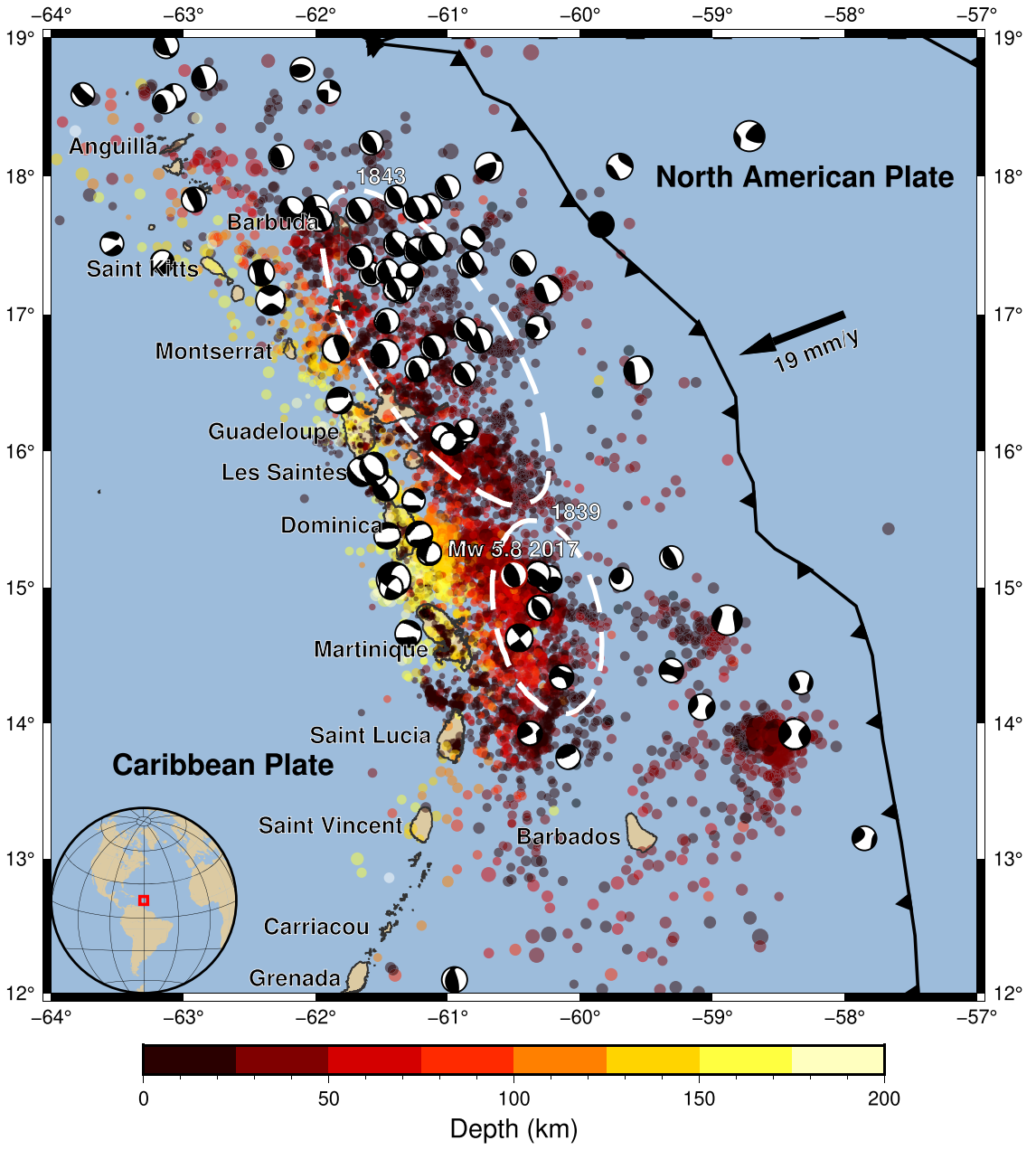

Figure 1. Seismicity of the Lesser Antilles Subduction Zone (LASZ). The dashed ellipses indicate the rupture area of the 1839 and 1843 earthquakes, inferred by Feuillet *et al.* (2011). The circles, coloured by depth, are the hypocentres from the unified catalogue of the IPGP French observatories (OVSG & OVSM 2020), between 01/01/2014 and 31/12/2019. Focal mechanisms, from GlobalCMT (Dziewonski *et al.* 1981; Ekström *et al.* 2012), are for *M*5+ earthquakes between 1978 and 2019. Focal mechanism for the 03/02/2017 M_w 5.8 event is from SCARDEC (Vallée *et al.* 2011).

Historical events in the region confirm the possibility of a megathrust earthquake generation in LASZ. Feuillet *et al.* (2011) compiled the data from several reports and papers for all significant historical earthquakes in the Lesser Antilles. They concluded that the magnitudes of the 1839 and the 1946 earthquakes offshore Martinique (Fig. 1) should be in the range of 7–8, based on regional intensity reports. Moreover, Weil-Accardo *et al.* (2016) studied the sea level changes over the last two centuries by analysing morphological changes of microatolls in eastern offshore Martinique. They underlined the strong possibility of magnitude 7 or more for both historical earthquakes.

Great population density in Martinique leaves it vulnerable to high risk in case of unpreparedness for a $M > 7$ earthquake (Audru *et al.* 2013). In the absence of a regional seismic hazard study, ground motion prediction by numerical modelling can guide future mitigation studies. The conventional approach in seismic hazard assessment is the use of ground motion prediction equations (GMPE) that provide estimation of peak ground motion at a distance (Douglas 2003). A GMPE is developed based on statistical data, and the paucity of large events in LASZ renders a regional GMPE development difficult in Lesser Antilles. Indeed, the only available GMPE, the 'B3' model of Beauducel *et al.* (2011), is limited to events of

magnitude less than 6.3. As an alternative to GMPE, numerical modelling offers the possibility of better understanding the physical aspect of the phenomenon (i.e. earthquake source and wave propagation). It allows for testing the outcomes of different configurations, which is particularly important for moderately seismic areas such as LASZ.

The challenge in numerical modelling is the uncertainty associated with model or input parameters, in particular when working with limited knowledge on earthquake process. The uncertainty related to earthquake source parameters can bring significant variations in the modelled ground motion (e.g. Ripperger *et al.* 2008; Imperatori & Mai 2012; Spudich *et al.* 2019). This impact is also valid in backward modelling. For example, as shown in Ragon *et al.* (2019) by their analyses on the 2016 Amatrice, Italy earthquake, accounting for uncertainties of only fault geometry can drastically control the estimated fault slip.

Our main objective is to identify the major factors related to earthquake source that control the ground motion amplitudes in Martinique during a potential M_w 7.5 interplate thrust earthquake. Within this objective, we prepared 320 rupture scenarios by varying kinematic features of the target hypothetical earthquake. For each scenario, we coupled fault rupture with empirical Green's functions (EGF) for seismic wave propagation, and predicted broad-band ground motion (0.5–25 Hz) at four stations of Martinique. Past studies (e.g. Ameri *et al.* 2009; Hartzell *et al.* 2002; Pacor *et al.* 2017; Sørensen *et al.* 2007; Wang *et al.* 2009; Withers *et al.* 2019) underlined the significant effect of source parameters on ground motion—for example, spatial variations of ground motion amplitudes due to rupture directivity or the location of slip asperities—and the necessity of considering the variability of source parameters when modelling ground motion. Here, we take forward these studies by considering a comprehensive set of source parameters and performing analyses in a broader frequency range.

The secondary objective is to test the role of EGF selection on predicted ground motion. The EGF approach emerges as a powerful method to model broad-band ground motion, especially when no detailed knowledge on propagation path is available, as revealed by many applications in the literature (e.g. Kamae & Irikura 1998; Pulido *et al.* 2004; Causse *et al.* 2009; Courboulex *et al.* 2010; Del Gaudio *et al.* 2018). It also takes into account possible site effects (except for soil non-linearity) and provides full time histories of ground motion, differently than GMPEs. On the other hand, among the applications in actively seismic areas, EGFs can be selected from foreshocks or aftershocks of a specific earthquake (e.g. Del Gaudio *et al.* 2015; Dujardin *et al.* 2016). Here, we study a moderately active zone with no successive recordings of such smaller events. In this case, selected events can differ more by several aspects such as seismic moment, stress drop, hypocentre location, etc. As Pavic *et al.* (2000) denoted, due to such differences between selected EGFs, further variation in ground motion can arise from the EGF method itself. Therefore, we also questioned the influence of EGF selection on ground motion.

Scoping these two objectives, the paper is structured as follows: (1) we detail the methods that we used for modelling source kinematics and wave propagation; (2) we explain how we constructed the set of earthquake scenarios and selected moderate earthquakes to use as EGF; (3) we address the following three questions, respectively: 'Which aspect(s) of the source control the ground motion, and why?'; 'How important is such a source impact on ground motion with respect to the GMPE?'; 'Is the EGF selection another significant factor to account for ground motion prediction?' and (4) we discuss the limitations of our study and present the main conclusions.

2 METHODS

We model the target interplate M_w 7.5 earthquake by using the kinematic source model of Ruiz's integral kinematics (RIK, Ruiz *et al.* 2011). RIK model generates, for an earthquake with a prescribed seismic moment, a stochastic slip distribution along with the full slip history—the source–time functions (STF)— at each node of a discretized fault plane. We convolve the output STFs with EGFs to compute ground motion at four stations of Martinique. In the following are given the main features of the RIK and EGF methods, respectively.

2.1 RIK model

We performed kinematic rupture modelling by using the RIK model implementation of Gallovič (2016). Slight modifications of the original RIK method issued by this implementation are also present here. The numerical tool that we used is an open source code (see Section 'Data Availability').

RIK is a composite model that describes an earthquake as a hierarchical set of smaller earthquakes, by definition of Frankel (1991). The essential idea behind the development of composite models is to represent the seismicity as a cascade of subsources standing for a wide range of wavelengths (Andrews 1980), and to mimic the high-frequency ω^{-2} decay (ω, being the angular frequency) of far-field displacement spectrum in observations (Aki 1967; Brune 1970), and in dynamic models of circular cracks (e.g. Madariaga & Ruiz 2016). A detailed review on the evolution of composite models can be found in Ruiz *et al.* (2011).

The number of sub-sources depends on their size, which follows a fractal distribution: the number of subsources with radius greater than a given size is:

$$N = \sum_{i=SUB_{\min}}^{SUB_{\max}} (2i-1)\frac{L}{W}, \tag{1}$$

where L is fault length; W is fault width; $SUB_{\min}$ and $SUB_{\max}$ are lower and upper limits of the ratio of fault width to subsource diameter, respectively.

Each sub-source is a circular fault, or crack—by definition of Eshelby (1957)—that is associated with a slip function of Δu, as follows:

$$\Delta u(r) = \frac{24}{7\pi}\frac{\Delta\sigma}{\mu}\sqrt{R^2 - r^2}, \tag{2}$$

where $\Delta\sigma$ is the static stress drop; μ is the shear modulus; r is the radial distance to the subsource centre and R is the subsource radius. The formula is valid for $r < R$; slip is zero outside the crack.

In the RIK model, the ω^{-2} decay results from imposing a slip-velocity function with a scale-dependent rise time $\tau(R)$ (Ruiz *et al.* 2011):

$$\tau(R) = \begin{cases} \dfrac{\alpha L_0}{V_r}, & \text{if } 2R > L_0 \\ \dfrac{\alpha(2R)}{V_r}, & \text{if } 2R \le L_0 \end{cases}, \tag{3}$$

where R is the subsource radius, α is a constant, that we set to 1 in this study; L_0 is a threshold of pulse width and V_r is the rupture speed.

The scale dependency of rise time only applies for the subsources with diameter smaller than L_0. This feature implies a low-pass filtering effect on the final slip spectrum.

The total slip rate of the modelled earthquake is obtained by summing the slip-rate contribution of each subsource. More details on the method can be found in Ruiz *et al.* (2011).

2.2 EGF

2.2.1 Formulation

We use the EGF method (Hartzell 1978; Irikura 1986) to model seismic wave propagation. This technique starts from the representation theorem of Aki & Richards (2002), which establishes a relationship between a fault rupture and the associated ground motion, based on Betti's theorem. The displacement, in the direction $\overrightarrow{x_n}$, u_n, at position x and time t, can be related to a discontinuity in the $\overrightarrow{x_p}$ direction of a fault plane Σ by the following integral:

$$u_n(x,t) = \int_\Sigma m_{pq}(\xi,\tau) * G_{np,q}(\xi,\tau;x,t)\mathrm{d}\Sigma, \tag{4}$$

where $\mathbf{m_{pq}}$ is the moment density tensor; $\mathbf{G}$ is the derivative of the Green's function tensor with respect to the direction $\overrightarrow{x_q}$ (along which the moment arm, or force separation, extends—seismic source is represented by a force couple here); and the symbol $*$ denotes time convolution.

Assuming that fault is embedded in a linearly elastic, isotropic medium, and each fault point has the same slip-time dependency, the moment density tensor can be simplified as follows:

$$m_{pq} = \mu(\xi)s(\xi,\tau)(\overrightarrow{s_p}\overrightarrow{n_q} + \overrightarrow{s_q}\overrightarrow{n_p}), \tag{5}$$

where μ is the shear modulus; $\mathbf{s}$ is the slip function; and $\overrightarrow{s}$ and $\overrightarrow{n}$ are the unit slip and fault-normal vectors, respectively, and the term between parentheses represents the focal mechanism of the causative fault.

Assuming that the radiated wave lengths are much greater than the fault dimension, eq. (4) can be written as follows:

$$u_n(x,t) = \int_\Sigma m_{pq}(\xi,\tau)\mathrm{d}\Sigma * G_{np,q}(\xi,\tau;x,t). \tag{6}$$

When replacing the integral of the above equation with the seismic moment of a real—EGF—event, M_0^{EGF}, it is possible to express the displacement-time history of an EGF event by the following convolution:

$$u_n^{\mathrm{EGF}}(x,t;\xi_0,\tau_0) = M_0^{\mathrm{EGF}}(\overrightarrow{s_p}\overrightarrow{n_q} + \overrightarrow{s_q}\overrightarrow{n_p})H(\tau-\tau_0) * G_{np,q}(\xi_0,\tau_0;x,t), \tag{7}$$

where $\mathbf{H}$ is the unit Heaviside function that stands for source–time function based on the assumption that the recorded wave periods are greater than rupture duration: Such an assumption means that the source is treated as a true point source—that has a negligible extent; ξ_0 and τ_0 are the hypocentre and the origin time of the EGF event, respectively.

We solve the displacement of the target event by the variational formulation of eq. (6) for a discretisized fault plane as follows:

$$u_n(x,t) = \sum_{ij}\mu^{ij}\cdot l\cdot w\cdot S^{ij}(\overrightarrow{s_p}\overrightarrow{n_q} + \overrightarrow{s_q}\overrightarrow{n_p})^{ij} * G^{ij}_{np,q}(\xi,\tau;x,t), \tag{8}$$

where l and w correspond to length and width of the unit area of the discretisized fault plane, respectively; S stands for the slip amplitude that is associated with the gridpoint (ij).

Assuming the same focal mechanism between the EGF and target events, and the same Green's function term for each fault segment, we can solve the above equation by using the EGF recording. Replacing the focal mechanism and Green's function term based on eq. (7), we rewrite the displacement of target event as follows:

$$u_n(x,t) = \sum_{ij}\frac{\mu^{ij}\cdot l\cdot w\cdot \tilde{S}^{ij}}{(M_0^{\mathrm{EGF}})^{ij}} * (u_n^{\mathrm{EGF}})^{ij}(x,t;\xi,\tau). \tag{9}$$

In this new formulation, $\tilde{S}$ stands for the slip function of the target event that is deconvolved by the step function of EGF.

The detailed explanation of the assumptions and derivation of above formula can be found in Aki & Richards (2002) and Hutchings & Viegas (2012).

We set the fault discretization after the assumption of self-similarity between EGF and target events (Aki 1967), which, in this definition, implies a similar stress drop for the small and large earthquakes, and proportionality between slip and rupture length. The following equation provides the scale factor between EGF and target event based on seismic moment:

$$n = \frac{L}{l} = \frac{W}{w} = \left(\frac{M_0^{\mathrm{target}}}{M_0^{\mathrm{EGF}}}\right)^{1/3}, \tag{10}$$

where L and W are the fault length and fault width of the target event, respectively; l and w are the length and width of unit area of the fault grid, respectively; M_0^{target} is the seismic moment of target event.

To satisfy the assumption of similarity between EGF and the target event in eq. (9), the two events should share the characteristics of focal mechanism, location and stress drop. Based on the applications of Del Gaudio *et al.* (2015, 2018), an earthquake should satisfy the following criteria to be used as EGF: (1) its location should be close enough to that of the target event; (2) its focal mechanism should be compatible to that of the target event (difference of faulting angles must be less than 15° and 30° for dip and strike, respectively) and (3) its magnitude should allow for a sufficient signal-to-noise ratio; and, at the same time, it should be at least 2 points smaller than the target magnitude to comply with the point source assumption in eq. (7).

2.2.2 Single-EGF versus Multi-EGF approaches

The difference between the single- and multi-EGF approaches lies in the way one associates the gridpoints of the fault plane with EGF(s): in the single-EGF approach, all the gridpoints use the same EGF for convolution; in the multi-EGF approach, the nearest EGF to gridpoint is used.

The multi-EGF approach can provide a better approximation of observations, as evidenced by past studies (Del Gaudio *et al.* 2015, 2018; McGuire & Ben-Zion 2017). As mentioned in Section 1, in case of scarcity of successive recordings, the difference of focal mechanism between the potential EGF events can critically increase such that EGF selection can become another factor causing further variation in predicted ground motion. Therefore, given the moderate seismicity of the studied zone, we considered both approaches in our analyses for further comparison.

The multi-EGF approach requires a few corrections to bring all the EGFs to an equivalent energy level and to account for differences between d^{point} (distance between station and gridpoint) and d^{hypo} (distance between station and EGF hypocentre). We apply the following steps:

(i) Adjustment of EGF spectra to the same shape (see Section 3.3.1).

(ii) Correction of differences in geometrical spreading: each convolution term, for each gridpoint, is multiplied by $d^{\text{point}}/d^{\text{hypo}}$.

(iii) Time-shift correction: for each gridpoint, the source time function is shifted by:

$$t_{\text{shift}} = \frac{d^{\text{point}} - d^{\text{hypo}}}{\beta}, \tag{11}$$

where β is average shear velocity. We use $\beta = 4.5$ km s^{-1}, which is the average *S*-wave value from Paulatto *et al.* (2017) tomographic model in the 35–55 km depth range, where the synthetic faults are placed (see next section). The approximation in eq. (11) is sufficient when the EGF signals are dominated by *S* phase as in our study (see supporting figures in Supporting Informations).

3 EGF SELECTION AND EARTHQUAKE SCENARIOS

In this section, we detail the procedure that we followed to select and correct the EGFs, and the preparation of earthquake scenarios.

3.1 EGF selection

We extracted from the catalogue of the IPGP Lesser Antilles observatories (see Section 'Data Availability') 423 events, between 01/01/2014 and 02/06/2018, whose epicentral locations are within a polygon offshore Martinique, as shown in Fig. 2. The depth of the selected events range between 0 and 196 km. The events follow the general trends of the subduction zone in terms of depth: they advent as a mix of crustal, interface, and intraplate events (see the discussion in Section 1). Thus, it is important to closely examine their depth and focal mechanism.

The catalogue only comprises events which have been recorded at each of the four broad-band stations of the 'West Indies' network in Martinique (WI, IPGP 2008c; Anglade *et al.* 2015): BIM, ILAM, MPOM and SAM (station locations shown in Fig. 3). We have limited knowledge of site conditions, essentially based on geological maps (Bureau de recherches géologiques et minières 2018): ILAM and MPOM are on rock, BIM and SAM are on soft soils (SAM is on volcanic ash and pyroclastic flow deposits), and site effects can be present at BIM and ILAM.

Out of the 423 events in our initial catalogue, only three could be selected as EGFs, based on the criteria of distance, magnitude, and focal mechanism discussed in Section 2.2.1. In particular, the desired EGFs: (i) are located, in depth, in proximity to the subduction zone, as does the M_w 5.8 earthquake of 03/02/2017 that we use as reference; (ii) have a magnitude in the interval of 3.5–5.5; (iii) have a focal mechanism of reverse faulting, and sticking to the flat-thrust characteristic of our target event, we only searched for events in the depth range of 25–65 km. Fig. 3 show the locations of the three events that satisfy these criteria while Table 1 provides details on these EGFs. Details on the determination of focal mechanism of the catalogued events are provided in Supporting Information. Moreover, note that, at the moment of submitting this article, a new solution for EGF II was made available in the catalogue—event `ipgp2017hushqz` (Section 'Data Availability'), with a slightly different location; we tested the effect of using this new solution on ground motion variation and verified the validity of the conclusions of the present work, as detailed in Supporting Information.

We determined the source properties of the selected three events (moment magnitude, corner frequency and stress drop) by using the SourceSpec software (Satriano 2021). SourceSpec calculates the earthquake source parameters for an event by inverting the *S*-wave displacement spectra from the recordings of multiple stations. The mean values of source parameters are computed by the average of the results of all the stations. The standard deviation of each parameter is also calculated; it can increase due to certain factors such as local soil conditions and/or poor signal quality at station. Therefore, we used all available data (stations from networks CU, G, GL, MQ, NA and WI; network information is detailed in Section 'Data Availability') and disregarded the stations with relatively high deviation to increase the robustness of the solution. Table 1 also lists the results of moment magnitude M_w, corner frequency f_c, stress drop $\Delta\sigma$ for each selected EGF.

In the following, we will only consider moment magnitudes. Fig. 3 shows the relation between corner frequency and seismic moment of each event with respect to stress drop. The mean stress drop of each EGF is between 25 and 50 MPa, and align considerably well in the diagram.

3.2 Earthquake scenarios

We prepared a set of earthquake scenarios for an interplate M_w 7.5 earthquake, comprising of 320 different kinematic rupture models. To take into account different aspects of source kinematics, we constructed a logic tree where each branch explores a different source parameter (Fig. 4). In the following, we briefly explain these aspects by hierarchical order.

3.2.1 Fault geometry

The logic tree starts with the main branches of fault geometry. We created two models: (1) a fault with a low aspect ratio (square-like) with dimensions of 50 km × 40 km; (2) a fault with a high-aspect ratio (rectangular) with dimensions of 80 km × 25 km. We set the model dimensions based on the scaling law of seismic moment for a magnitude 7.5 event such that the two cases have the same rupture area.

We fixed the fault location and orientation based on a reference event, the 03/02/2017 M_w 5.8 earthquake (Fig. 3). The focal mechanism of this event was reported as reverse faulting with strike, dip and rake angles of 161°, 30° and 94°, respectively, and hypocentre is located at 46 km depth (SCARDEC data by Vallée *et al.* 2011). We set our maximum fault depth to 55 km in all cases, by respecting the past documentation on the seismogenic zone (e.g. Paulatto *et al.* 2017). As for the updip fault limit, we consider here a rupture occurring at the slab-mantle wedge interface, where most of the large *M*5+ interplate earthquakes and background seismicity occur (Fig. 1), as also evidenced by Paulatto *et al.* (2017). Similarly to what happens for the Japan trench (Satriano *et al.* 2014), *M*7 earthquakes occurring deeper but closer to the coast, are susceptible to generate stronger ground motion. We defined the midpoint of the first type of fault geometry at the hypocentre coordinates of the 03/02/2017 event (15.090°N, 60.504°W). In this way, the fault plane extends between 35–55 km and 42.5–55 km depths for the first and second types of geometries, respectively. Fig. 3 depicts the location of two fault geometries in map view and cross section. The alignment of fault planes are slightly shallower with respect to the slab, but in good agreement with the depth of recorded events.

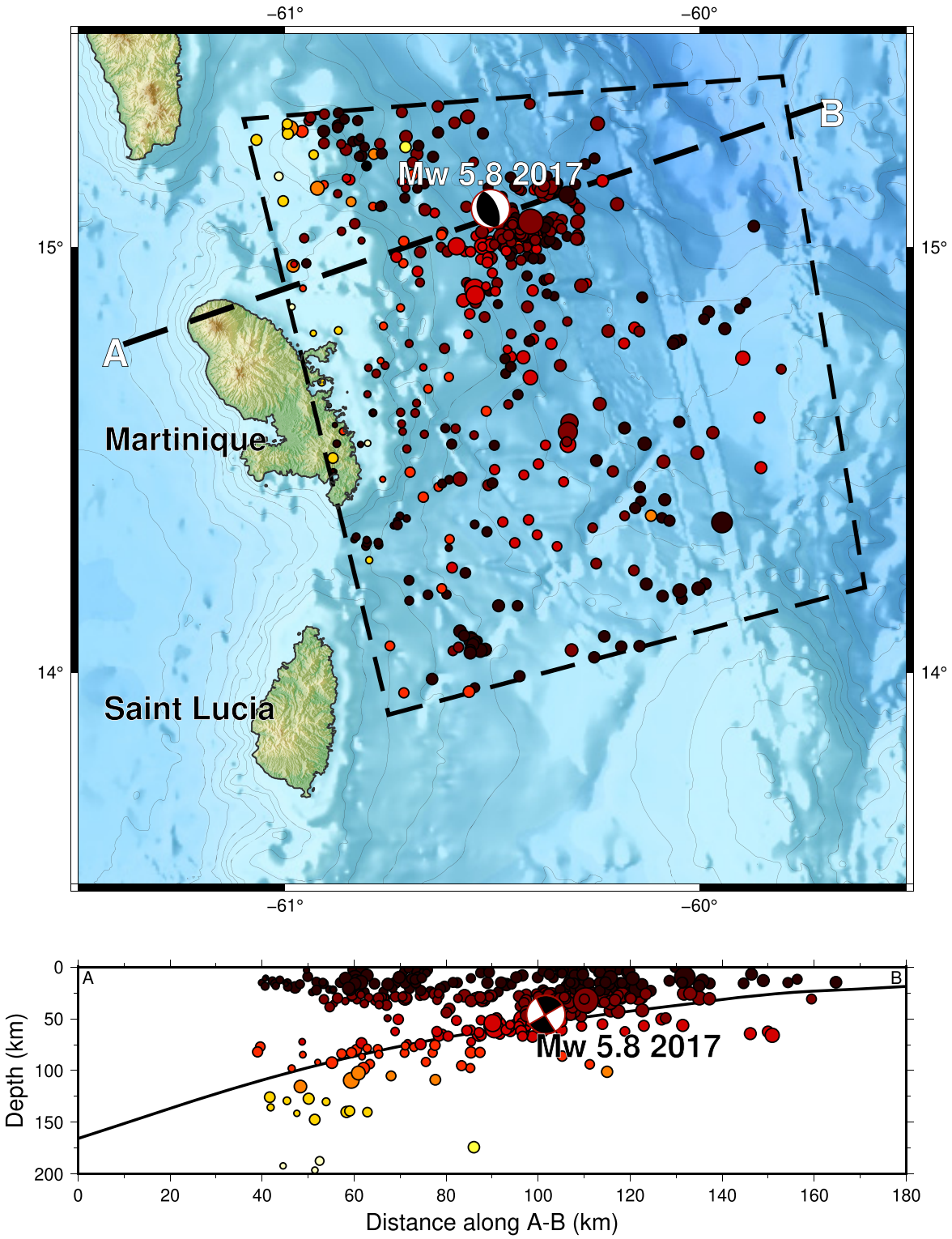

Figure 2. Seismic catalogue selected for this study. The dashed polygon represents the geographical selection; hypocentres within this polygon are only of those recorded by the four broad-band stations in Martinique. These hypocentres are also shown on the vertical cross-section, along with the slab model of Paulatto *et al.* (2017). Focal mechanism for the 03/02/2017 M_w 5.8 event is from SCARDEC (Vallée *et al.* 2011).

3.2.2 Spatial distribution of subsources

We created two sub-branches to test the effect of using uniform or dip-varying spatial distribution of large sub-sources. In uniform-distribution model, we evenly distributed the subsources all over the fault plane; in dip-varying distribution model, we define the along-dip probability to have a subsource as:

$$P(d) = \cos^9\left(\frac{\pi d}{2W}\right),$$

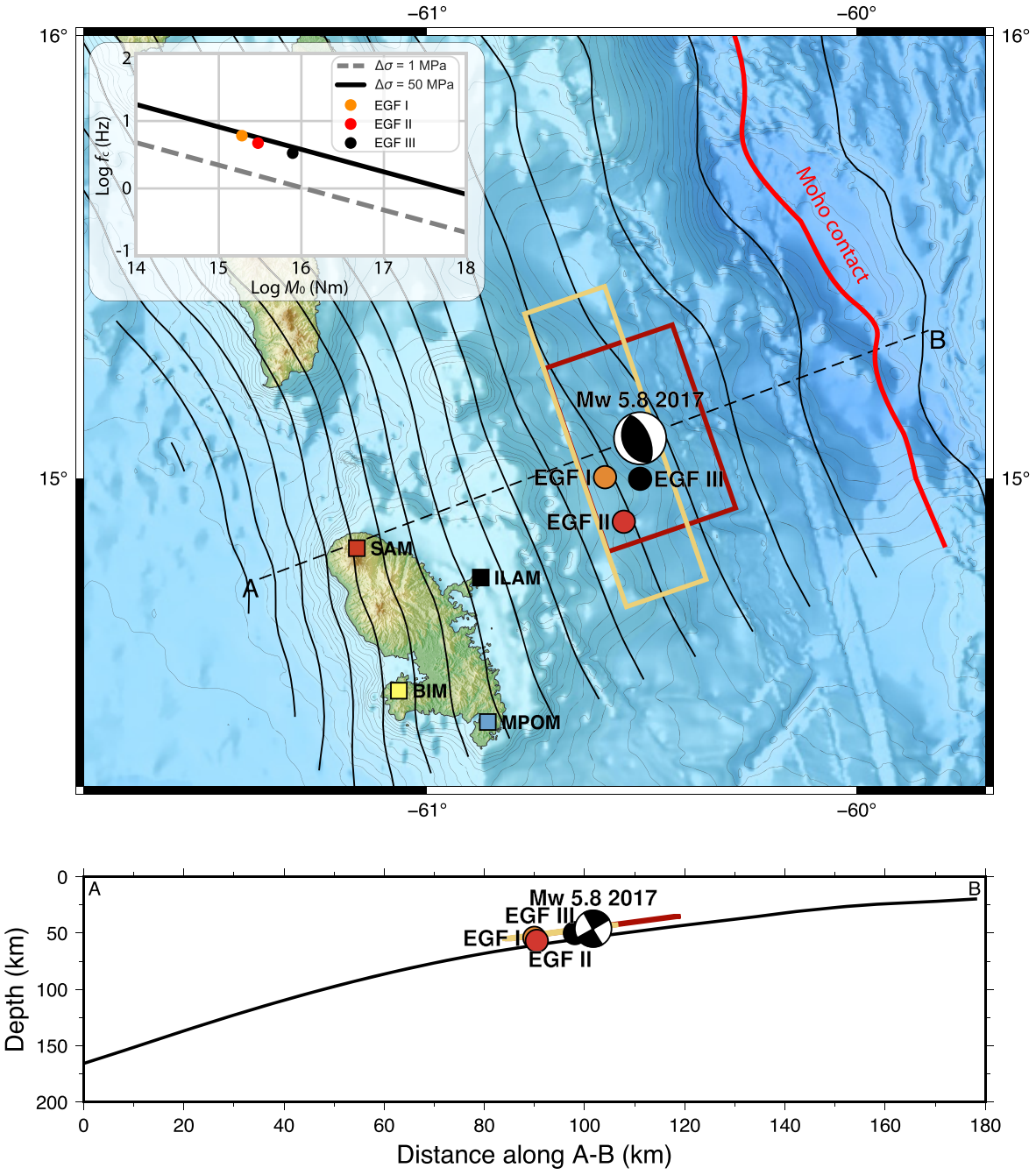

Figure 3. Source and station locations, and source properties of the selected EGFs. Map view of the four selected Martinique stations (WI network), the two fault geometries, the selected EGF events and the focal mechanism of the 2017 M_w 5.8 earthquake (top), and vertical section showing the EGFs and the 2017 focal mechanism (bottom). The slab geometry from Paulatto *et al.* (2017) is represented by contour lines (10 km depth interval) in map view and by the solid line in the depth section. The red line in the map view marks the contact between the overriding plate Moho and the slab, according to Paulatto *et al.* (2017). Embedded figure displays the corner frequency versus seismic moment for each selected EGF.

Table 1. Catalogue information (ID, origin time, location, M_L) for the EGFs used in this study and source properties (M_w, f_c, $\Delta\sigma$) obtained from SourceSpec analysis.

EGF	Catalogue ID	Origin time (UTC)	Lon. (°E)	Lat. (°N)	Depth (km)	M_L	M_w	f_c (Hz)	$\Delta\sigma$ (MPa)
I	ipgp2016fkyaql	2016-03-17T18:31:26	–60.56	15.00	54.1	4.12	4.1 ± 0.2	6 ± 2	40 ± 28
II	ipgp2017hushqx	2017-04-21T10:13:01	–60.54	14.90	56.8	4.82	4.3 ± 0.2	5 ± 2	29 ± 22
III	ipgp2017seplqt	2017-09-15T10:58:31	–60.50	15.00	50.0	5.04	4.5 ± 0.3	3 ± 2	27 ± 23

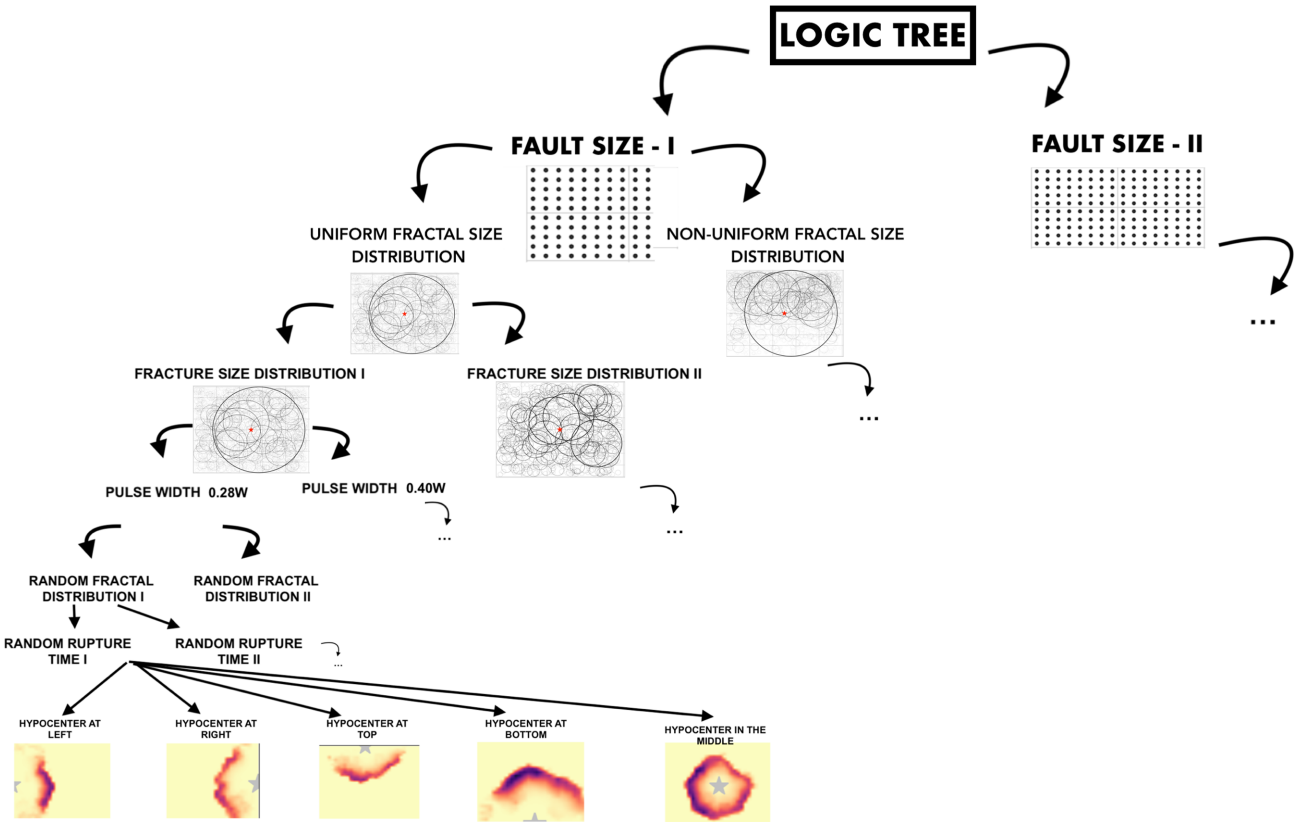

Figure 4. Illustration of the logic tree organization for generating earthquake scenarios. Three dots indicate the repetition of sub-branches similar to those of neighbour branch.

where d is the along-dip distance and W is fault width: $P(0) = 1$ at fault top; $P(W) = 0$ at fault bottom. The power of nine was arbitrarily chosen to increase the relative probability close to the fault top with respect to the fault bottom. From this probability function, we define a subsource size-dependent probability

$$\bar{P}(R, d) = P(d)^{\gamma(R)}$$
$$\gamma(R) = \frac{R - R_{\min}}{R_{\max} - R_{\min}}.$$

Hence, for the largest subsource, the probability density function equals $P(d)$; and for the smallest one it equals 1, that is being uniform over the fault plane.

3.2.3 Subsource size

We tested the effect of the presence of the largest subsource, with diameter equal to fault width. The first sub-branch allows for a relatively large range of subsource sizes: the largest and smallest radii equal 100 and 5 per cent of fault width, respectively. We lowered the largest radius to 50 per cent in the second group.

3.2.4 Pulse width, L_0

As mentioned in Section 2.1, this parameter produces a low-pass filtering effect on slip spectrum, and hence can influence the ground motion amplitude. We tested the power of such influence by adding two sub-branches: (1) $L_0 = 0.28 \times W$; (2) $L_0 = 0.4 \times W$. The use of very small values of L_0 can lead to unrealistically high ground motion amplitudes, such as PGA exceeding 2 g; We opted for the L_0 values for these two cases after a sensitivity analysis of the parameter on PGA (detailed in Supporting Information).

3.2.5 Random parameters, `idum1` and `idum2`

The numerical tool that we use incorporates two parameters, `idum1` and `idum2`, that control the randomness of the spatial distribution of subsources and propagation of rupture front on fault grid, respectively. We created two additional orders of sub-branches to account for each of this randomness.

3.2.6 Rupture directivity

We created a last order of sub-branches to test the effect of rupture directivity, by varying the hypocentre location. We prepared five cases based on the relative location of hypocentre on fault plane: left, right, top, bottom and centre.

3.3 EGF correction and coupling with kinematic rupture model

3.3.1 EGF correction

We adjusted all selected EGFs to the same spectral shape that corresponds to a reference spectrum for a M_w 4.3 event, with a seismic moment of 3.6×10^{15} Nm. The philosophy of EGF correction is to reduce significant variation of ground motion amplitudes that can possibly arise from the difference of stress drop of selected EGFs (Hutchings *et al.* 2007; Del Gaudio *et al.* 2015). We set the corner

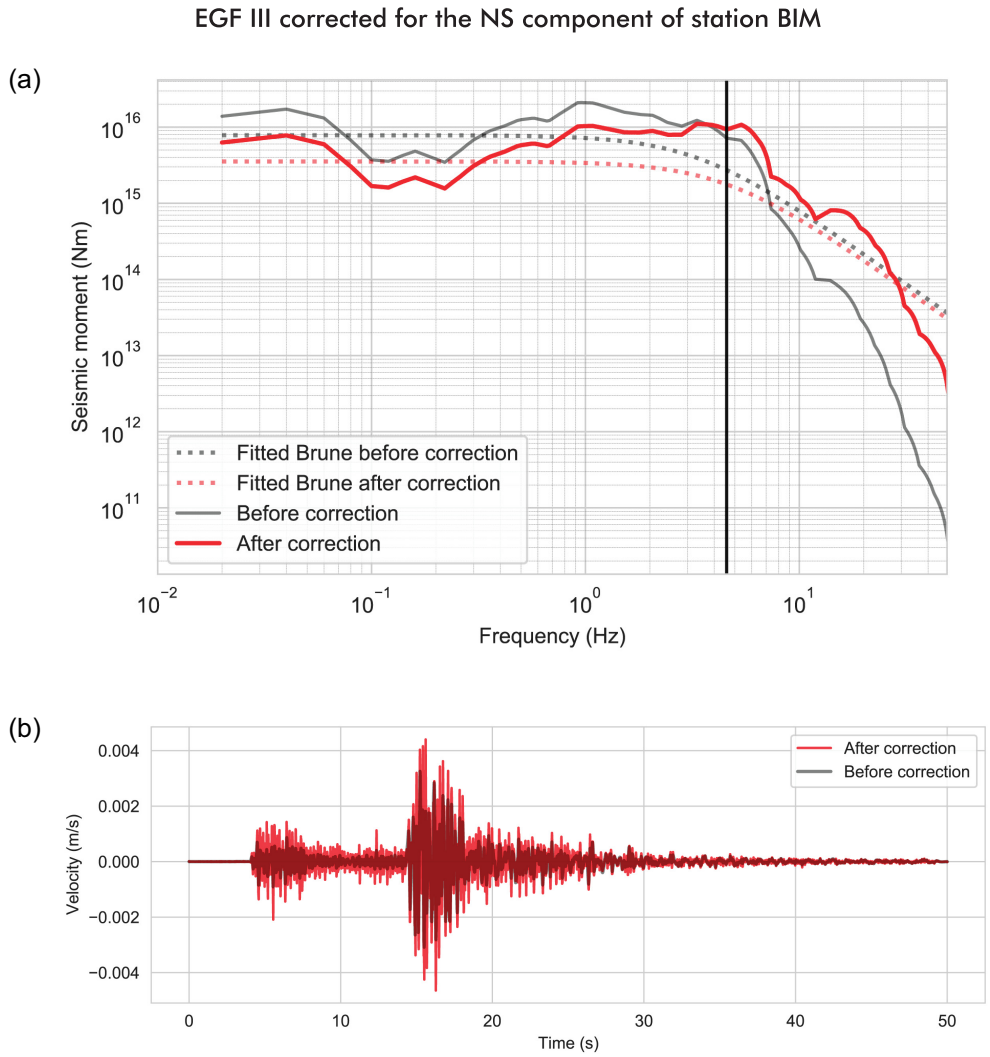

Figure 5. Example of EGF correction. (a) Moment spectra of the north-south component of EGF III signal at station BIM before and after correction. (b) Velocity-time histories before and after correction.

frequency of the reference spectrum to the mean of EGFs' values, that roughly equals 5 Hz. For each station record of each EGF, the adjustment procedure applies as follows:

(i) Computation of the Fourier transform of displacement.
(ii) Conversion of displacement spectrum to seismic moment unit.
(iii) Deconvolution (amplitude division) of the converted spectrum by Brune's spectrum that corresponds to the corner frequency and seismic moment of the uncorrected EGF—this step is similar to the application in Causse *et al.* (2017).
(iv) Multiplication of the deconvolved spectrum by the seismic moment value chosen for the reference spectrum.

Generally, the EGF summation technique in eq. (9) is applied up to the EGF's corner frequency (Hartzell 1978), above which the solution has larger uncertainties. This is mainly because the point-source assumption in eq. (7) is satisfied with a flat amplitude spectrum, while the observed spectrum is not flat above the corner frequency. The EGF deconvolution by a Brune's spectrum only partially recovers a flat amplitude spectrum: the Brune's model is not fully adequate in describing high-frequency radiation, since it assumes an instantaneous rupture on a circular fault, which is a good approximation only below the corner frequency (Madariaga & Ruiz 2016). For higher frequencies, the spectrum of any earthquake deviates—in amplitude and phase—from the Brune's model: the seismic radiation at high frequencies is inherently stochastic, since the different portions of the rupture interfere with each other. This stochastic behaviour is therefore still present after the Brune's spectrum deconvolution and the EGF summation can result in constructive/destructive interference above the corner frequency, depending on the high-frequency spectrum shape of the (corrected) EGFs. We further discuss the limitation arising from this application in next section.

It's worth noting that we preserve the attenuation information on the final spectrum by not including anelastic (and geometric) attenuation in the Brune's spectrum which is deconvolved in step (iii). Final step of signal processing includes: removal of instrumental response, detrending and bandpass filtering in the frequency band of 0.01–49 Hz.

Fig. 5(a) shows an example of spectral adjustment of EGF III for the north–south component of station BIM. All the spectra are smoothed with a Hanning window of the 5th degree. We see in

the example that the spectrum is deamplified after correction at frequencies below the corner frequency of reference spectrum (∼5 Hz) since the seismic moment of the uncorrected EGF is higher than the reference one. The flattening effect of EGF adjustment beyond corner frequency produces an amplification at frequencies above ∼5 Hz; however, due to the preserved anelastic attenuation, the resultant spectrum still shows a decay for frequencies above ∼6 Hz. The resulting signal in time domain depicts notable amplification—up to two times for peak values—throughout the signal duration due to correction, as shown in Fig. 5(b).

3.3.2 Coupling with kinematic rupture model

We discretisized the fault plane based on the ratio of seismic moment between the target and EGF events, that equals 40. Referring to eq. (10), our fault grid contains 1600 points (40×40 for $n = 40$) for all rupture models.

For each gridpoint, the corresponding source time function is convolved with the nearest EGF in 3-D space. One example of such partition for the case of a fault with low-aspect ratio (the 1st type of fault geometry in the logic tree) is given in Supporting Information (Fig. S1). We then made additional corrections as detailed in Section 2.2.2. The modelled ground motion at a station issued by the target earthquake equals the sum of the corrected convolutions. The velocity and density profile that we used is provided in Supporting Information.

The frequency band which we considered for ground motion modelling is 0.5–25 Hz, based on signal quality. We further analysed the signal-to-noise ratio (SNR) of each EGF recordings for each station. Except for the cases with slightly lower SNR values, all the cases provide SNR values above 5 in the frequency band of 0.5–25 Hz. Therefore, we will refer to this frequency band in the evaluation of our ground motion models.

The main limitation of our modelling approach is that the EGF has a corner frequency of 5 Hz, that is smaller than the above-mentioned resolution, 25 Hz. As detailed in the previous section, the EGF deconvolution by a Brune's spectrum does not mitigate interference effects arising from rupture stochasticity and, hence, the uncertainties associated with the modelled ground motion are higher above the EGF's corner frequency. Causse *et al.* (2009) discuss that such stochastic effects can lead to overestimation of high frequency level of apparent source–time function in case of constructive interference. Here we verified the lack of such artefacts in our models as exemplified in Fig. S2. We note and consider this limitation when interpreting our results in the following.

4 RESULTS

We evaluate the results for the 320 simulated scenarios, through the following parameters: peak-ground acceleration (PGA), spectral acceleration (SA) values at 1, 2 and 5 Hz and Arias intensity. We made these analyses on the maximum of the three components. Lancieri *et al.* (2015) showed that these are the most influential parameters on seismic structural analysis.

4.1 Fault geometry and subsource size control the ground motion prediction

The first question we wanted to address is: 'Which aspect(s) of the source control the ground motion?'. To answer this question, we evaluated the model outputs by considering each branch of the logic tree (Fig. 4). To account for both amplitude and energetic content of the calculated ground motion, we disaggregated the simulation results based on PGA and peak Arias intensity. Fig. 6 shows disaggregation for station ILAM (the analyses on the other stations lead to the same conclusion, as shown in Supporting Information). Our analyses on all four stations highlight a distinctive clustering due to the fault geometry and sub-source size: a low aspect ratio of fault geometry brings relatively low energetic ground motion (cluster A); whereas, a high aspect ratio of fault geometry together with smaller slip asperities—that is a rectangular fault where sub-sources larger than 50 per cent of fault width are forbidden—results in a notable amplification of peak ground motion (cluster B).

Such clustering implies a significant change of wave energy throughout the signal duration and in a broad frequency range (0.5–25 Hz). We picked a representative case from each of the above-mentioned two clusters A and B. We compared the two cases by acceleration-time histories, their Fourier amplitudes, and temporal change of Arias intensities. Fig. 7 displays this comparison for all stations. The cluster B case evicts a higher level of wave energy at all stations: PGA is approximately two times higher, and the peak Arias intensity can reach to 10 times higher values for all stations.

We found that the combination of a fault geometry with a high aspect ratio and a spatially condensed largest slip distribution, that is smaller patches with greater slip values, makes a double effect of amplification of source energy; and, this double energy boost leads to the clustering of ground motion. We compared the two clusters by sub-source distribution (i), final slip distribution (ii), and STF (moment-rate time function) and moment spectra (iii) (Fig. 8). Our analysis evidences that:

(i) The presence of the subsource with a diameter equal to fault width (cluster A) results in a spatially extensive slip asperity such that a significant part of the fault plane undergoes relatively large slip. Yet, the lack of such big-size subsource (cluster B) results in a slip distribution where the largest values are spatially concentrated in relatively small patches. This leads to a partial amplification of source energy in the whole frequency band, in particular above 1 Hz.

(ii) The fault geometry with high aspect ratio (cluster B) can result in a rupture propagation that is longer and in a composite source–time function with multiple peaks and shorter rise time—individual slip-rate functions become spiky (short rise time) in the cluster B case, differently than the case of cluster A that has smooth STFs (see details in Supporting Information). This complexity also partially contributes to the energy amplification in the whole frequency band.

4.2 Comparison with GMPE: source impact on ground motion determines the GMPE compatibility

The second question we wanted to address is: 'How important is the source-related changes in ground motion with respect to the GMPE?'. In previous section, we evidenced two clusters of synthetic ground motion due to the differences of source definition. Here, we evaluate this ground-motion clustering by referring to the compatibility of the modelled data with GMPE.

Bozzoni *et al.* (2011) compiled all the available databases in Eastern Caribbean Islands and analysed different GMPEs that have been developed for other regions with similar seismotectonic settings. They recommend the GMPE of Zhao *et al.* (2006) for the type of events we study here, namely plate interface earthquakes with a reverse faulting mechanism. A similar conclusion was made in a later study by Douglas & Mohais (2009). The GMPE of Zhao *et al.*

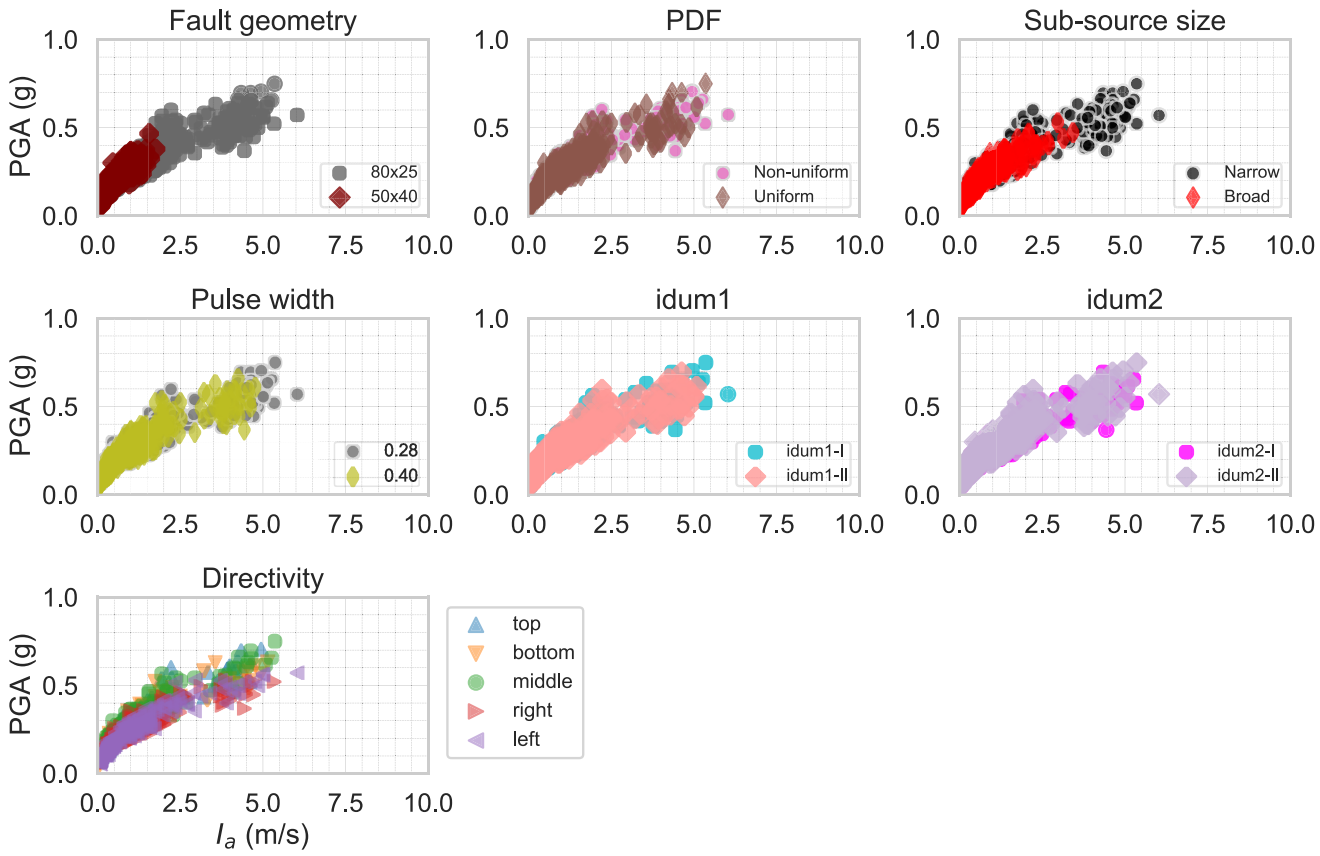

Figure 6. Disaggregation of computed ground motion by PGA and peak Arias intensity for station ILAM. We classified the results by different parameters in each diagram: by fault geometry, spatial distribution of subsources (PDF), subsource size, pulse width, `idum1`, `idum2` and directivity. The choice of fault geometry and subsource size parameters are the causative factors of two distinct clusters, which we call 'A' and 'B'.

(2006) consists of four soil categories: rock, hard soil, medium soil and soft soil. In the absence of a detailed knowledge on site conditions, we have chosen the site condition of soft soil. We verified by using other site conditions that this choice only causes slight variations of amplitude and does not change our conclusions (see figures in Supporting Information).

The two clusters of synthetic ground motion have two different levels of ground motion amplitude by distance. The compatibility of these trends with GMPE for M_w 7.5 strongly depends on frequency and station. Fig. 9 shows the comparison of synthetic ground motion and GMPE curves for spectral acceleration (SA) analyses at 1, 2 and 5 Hz. We make the comparison separately for each station, and the hypocentral distance at each simulation varies based on the definition of hypocentre. In general, cluster B is associated with higher amplitude of ground motion at all distances. At 1 Hz, the majority of the synthetic ground motion agrees well with GMPE for stations BIM and SAM; but, the ground motion at the same frequency is mostly underestimated for stations ILAM and MPOM. At 2 Hz, SAs for cluster A align with mean GMPE predictions for the stations BIM and SAM, whereas they are closer to lower limit of GMPE predictions for the other two stations. At 5 Hz, the cluster B mostly overestimates the GMPE predictions for all stations except for MPOM, and the agreement of the first cluster with GMPE remains station dependent. The comparative analysis of PGA prediction between the synthetic data and GMPEs gives the same conclusion as we show here for SA at 5 Hz: the synthetic data in cluster B overestimates the GMPE predictions for all stations, and the cluster A data mostly fall into the predicted range of GMPEs for only MPOM (Details can be found in Supporting Information).

Accounting for the limitation of ground motion modelling above the corner frequency of EGFs, that equals 5 Hz, we further verified whether our findings are still valid below that frequency. Our conclusions remain valid: ground motion amplitude is clustered in two groups, and the compatibility of the clusters with the GMPEs depends on both the station and the evaluated frequency (detailed in Supporting Information).

4.3 EGF selection can emerge as a significant station-dependent factor for ground motion prediction

The third question we aimed to address is: 'Does EGF selection further influence ground motion estimations?'. The analyses in previous sections were based on the multi-EGF approach in order to focus exclusively on the source effects. Here we explore the role of the EGF selection by repeating the logic tree simulations for each single-EGF use.

We found that the predicted ground motion can be highly sensitive to EGF selection: the energy difference of EGFs in a specific frequency band can cause significant variations in predicted ground motion despite the EGF corrections. We categorized the synthetic data by EGF use as shown in Fig. 10. Stations BIM, ILAM and MPOM exhibit notably higher ground motion amplitudes for the use of EGF III, while for station SAM such effect is not obvious.

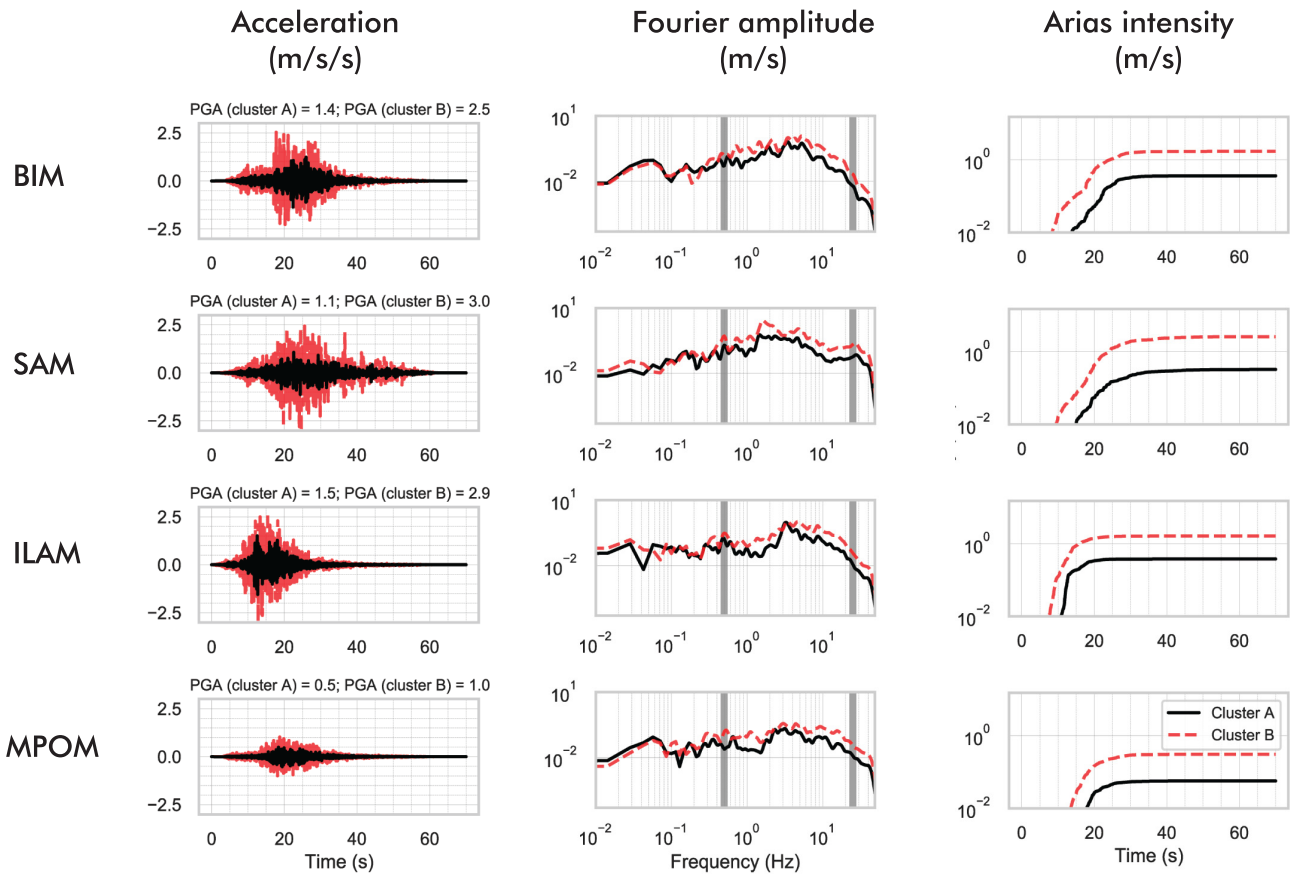

Figure 7. Comparison of acceleration-time histories (left-hand panel), Fourier amplitude (middle panel), and Arias intensities (right-hand panel) between cluster A (in black) and cluster B (in red) (see Fig. 6). We used the north–south component of signals in each comparison. Each row corresponds to the results of a station: BIM, SAM, ILAM and MPOM, from top to bottom, respectively. The frequency band of 0.5–25 Hz is indicated by grey bars.

5 DISCUSSION

5.1 Variation of ground motion between stations

The range of ground motion amplitude strongly varies between the four stations; In general, we computed a weaker ground motion amplitude for station MPOM compared to other stations. Fig. 11 shows histograms and kernel density estimations (KDE) of computed PGA for all performed simulations. KDE is a way of visualizing the shape of the sample distribution (Parzen 1962; Davis *et al.* 2011); it is defined as the normalized sum of kernel functions of a certain width computed on the data samples (here we use Gaussian kernels of standard deviation 0.10, 0.10, 0.11 and 0.04 g for stations BIM, SAM, ILAM and MPOM, respectively; details on KDE can be found in the reference provided in Section 'Data Availability'). The results point to a similarity between three stations, BIM, SAM and ILAM, in terms of amplitude and standard deviation. For both clusters, the mean values for the three stations are roughly twice as that of MPOM. For example, the mean PGA of the cluster A ranges between 0.2 and 0.22 g for the three stations, whereas this value lowers to 0.08 g for station MPOM. The peak kernel density notably increases, approximately twice, at station MPOM due to the narrow range of PGA, that is limited variation, compared to the other three stations.

A detailed site characterization is essential to better assess the variation potential of ground motion between the stations and understand the reason behind it. Recall that we found that the significance of ground motion variation with respect to GMPE and the potential of further variation due to EGF selection are station-dependent. Our current knowledge about site conditions is limited and does not allow for further interpretations of the variation of ground motion between stations in our results. Additional analyses to characterize site effects at Martinique stations—as applied in Guadeloupe (Castro *et al.* 2003)—would be helpful for future seismic hazard studies in Martinique. Moreover, EGF method considers a similarity of the source-to-site propagation path between EGF and target earthquake; it cannot account for further variation of ground motion due to possible site-related complexities due to a strong earthquake. We target a magnitude 7.5 earthquake, and further variation of ground motion due to complex soil behaviour (e.g. soil non-linearity and liquefaction) under such a strong earthquake is possible as known by past observations and numerical studies (e.g. Aguirre & Irikura 1997; Ghofrani *et al.* 2013; Régnier *et al.* 2013; Oral *et al.* 2019). Further research on this aspect, together with an enhanced site characterization, can take the effort of ground motion prediction a step forward.

5.2 Need for an improved regional GMPE

The absence of a regional GMPE for a magnitude 7.5 earthquake is another limitation for the interpretation of our results; the only regional GMPE, the 'B3' model (Beauducel *et al.* 2011), also needs revision for moderate events. Here we used the GMPE of Zhao *et al.*

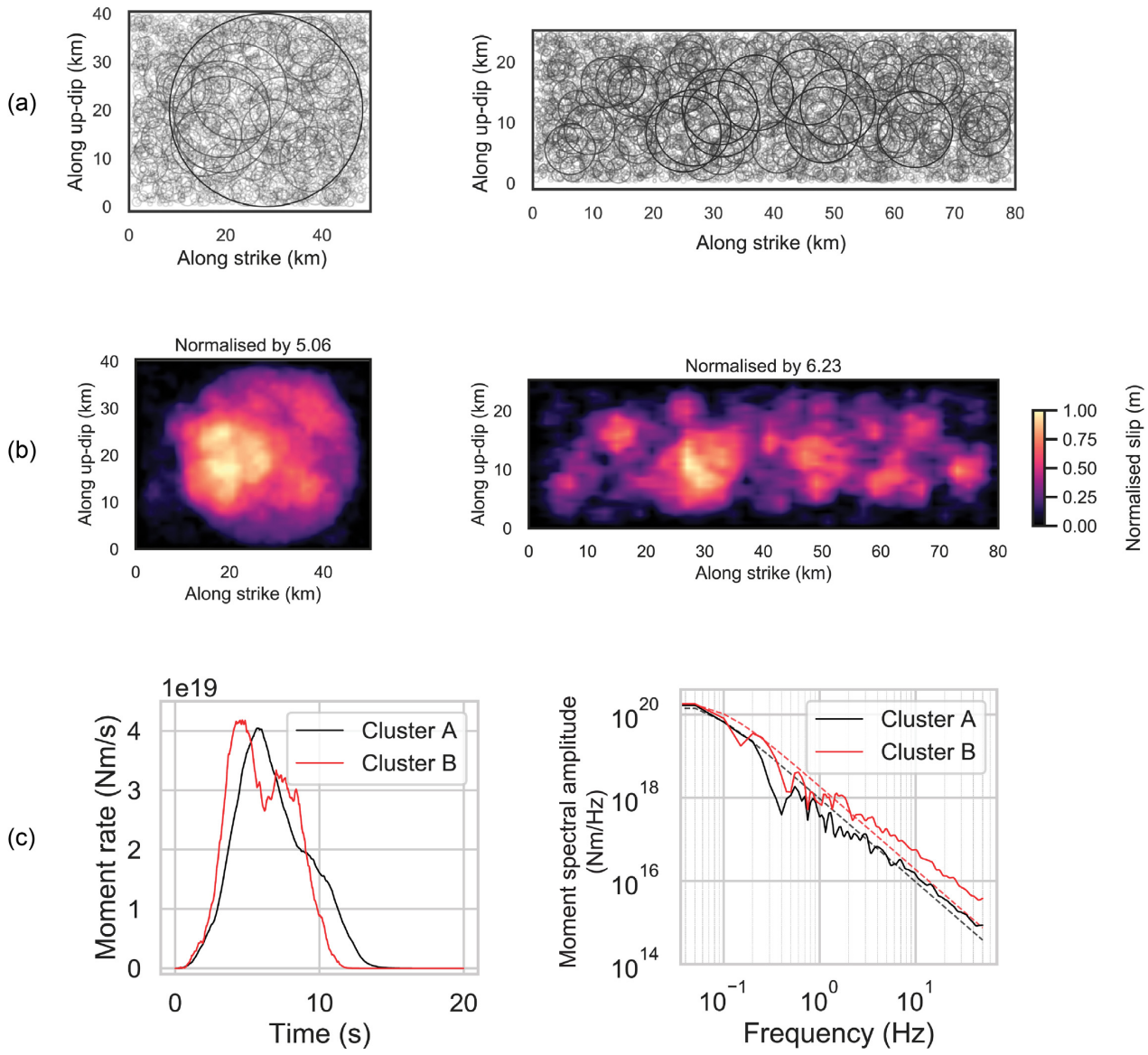

Figure 8. Comparison of source features of the two clusters shown in Fig. 6. (a) Comparison of cluster A (left-hand panel) and cluster B cases (right-hand panel) by subsource distribution. (b) Same as a for final slip distribution. (c) Comparison of source–time function (left-hand panel) and moment spectra (right-hand panel) between cluster A (in black) and cluster B (in red) cases.

(2006), that was developed with Japanese data, to analyse our synthetic ground motion data, since the B3 model is not recommended for $M \geq 6.5$ earthquakes. Although past studies qualify the Zhao *et al.* (2006) GMPE as the best representative of our target earthquake, Kotha (2018) states that the use of a GMPE that has been developed with the data from a different region can become non-ergodic due to the differences of crustal characteristics. Therefore, according to the latter, such GMPEs require additional adjustments of ground motion before application to other regions. In that sense, future mitigation studies would benefit from further research on GMPE applications.

We compared the B3 model and Zhao *et al.* (2006) GMPE with the EGF recordings, in a range of magnitudes (4.2–4.5) where both GMPEs are valid (Fig. 12). B3 model underestimates all the three events, whereas Zhao *et al.* (2006) is mostly in agreement with observations. This incompatibility also points to further need to improve regional GMPE applications.

6 CONCLUSIONS

A $M > 7$ interplate earthquake is expected offshore Martinique. In this study, we investigated the most influential parameters on broad-band ground motion mainly due to source kinematics for a hypothetical M_w 7.5 earthquake.

Our findings are:

(i) The fault geometry and the spatial extension of the largest slip patch are the most determinant source-related factors for ground motion. The combination of a rectangular fault with a high aspect ratio and condensed small slip asperities can result in a significant amplification of source energy. Such energy amplification manifests itself by a substantial increase of broad-band wave energy and ground motion amplitude throughout the signal duration. We stress that we set the downdip limit to 55 km, as suggested by Paulatto *et al.* (2017) for the coupled interface of the subduction zone; more

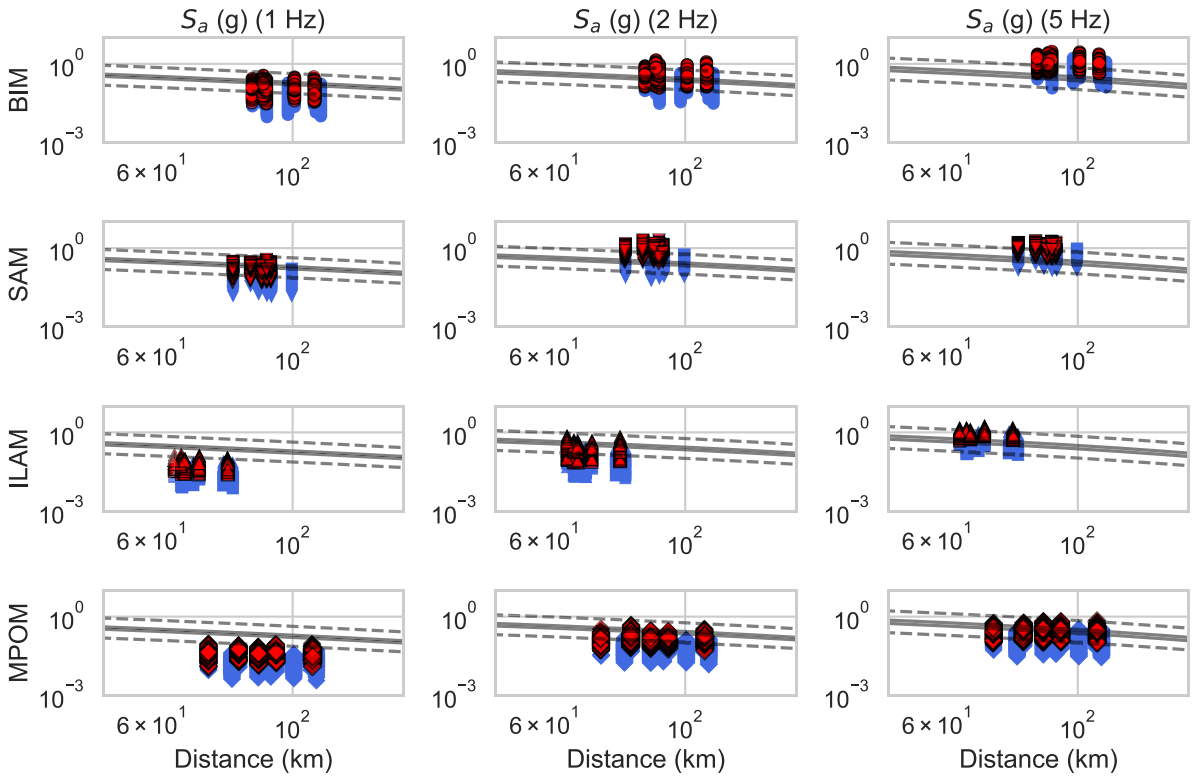

Figure 9. Comparison of cluster A (in blue) and cluster B (in red) cases of synthetic ground motion with GMPE curves from Zhao *et al.* (2006) (in gray) by spectral acceleration at 1 Hz (left-hand panel), 2 Hz (mid panel) and 5 Hz (right-hand panel). The results for 5 Hz mean GMPE curves are shown in solid lines; the lower and upper limits of GMPE curves are shown in dashed lines. Each row stands for the analysis of a station: BIM, SAM, ILAM and MPOM from top to bottom, respectively. We used soil class #4 for GMPEs.

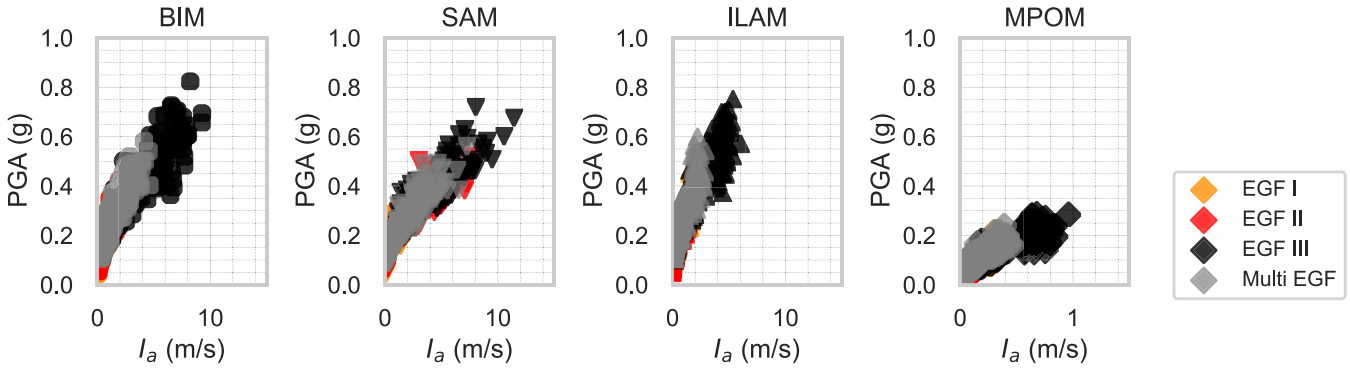

Figure 10. Effect of EGF selection on ground motion. Comparison of peak ground acceleration versus peak Arias intensity results between all EGF approaches. Each diagram shows the results for a station.

studies are needed to constrain the further role of the fault geometry when considering different depths of the downdip limit.

(ii) The agreement between simulated ground motion and GMPE estimations is highly sensitive to the evaluated frequency of ground motion and station. Future research on the improvement of regional GMPE application and site characterisation is necessary to constrain the realistic range of ground motion and source parameters.

(iii) EGF selection can be another factor causing significant variation in the predicted ground motion. The application of EGF technique for forward modelling in moderately seismic areas such as Martinique requires a special attention to EGF selection, because of potential energy differences between EGF events. Despite the broad-band ground motion modelling (0.5–25 Hz), we underline that the variability of our results is higher beyond the EGF corner frequency, that equals 5 Hz here, because of the stochastic nature of rupture at those frequencies. Thus, we put a special emphasis on the need for using more EGFs and a deeper look to rupture dynamics to better constrain the ground motion at such high frequencies.

ACKNOWLEDGEMENTS

This study is funded by the convention between Institut de physique du globe de Paris and General Directorate of Prevention of Risks of French Ministry for the Ecological and Solidarity Transition and by the project "Vers la Plateforme Régionale de Surveillance Tellurique du futur" (PREST) cofunded by INTERREG Caraïbes through the European Regional Development Fund.

We would like thank to Sergio Del Gaudio, František Gallovič and Jean-Marie Saurel for their substantial help in applying the

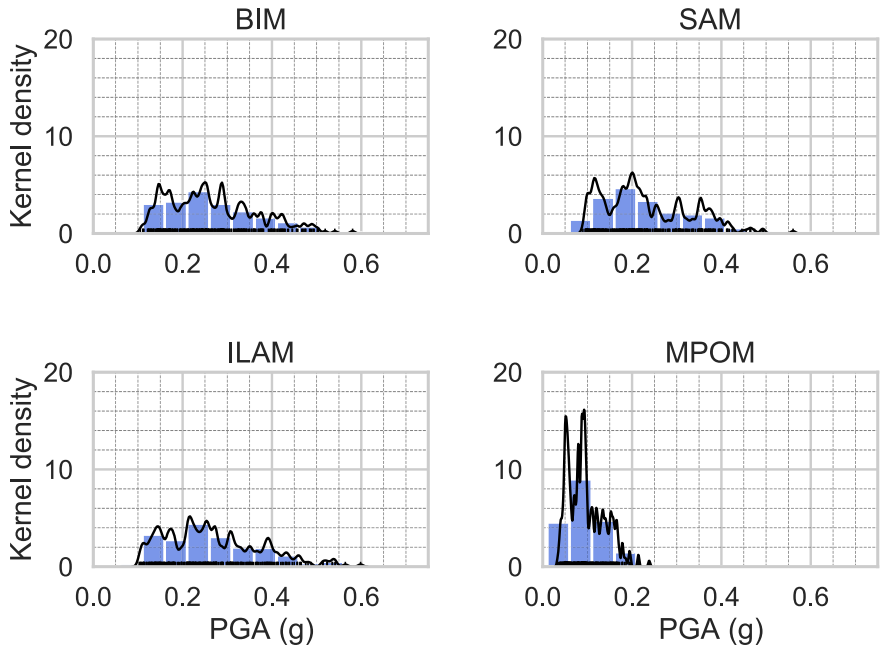

Figure 11. Histograms of peak ground acceleration values at each station, associated with kernel density (black curve). Each rug stands for a simulation result.

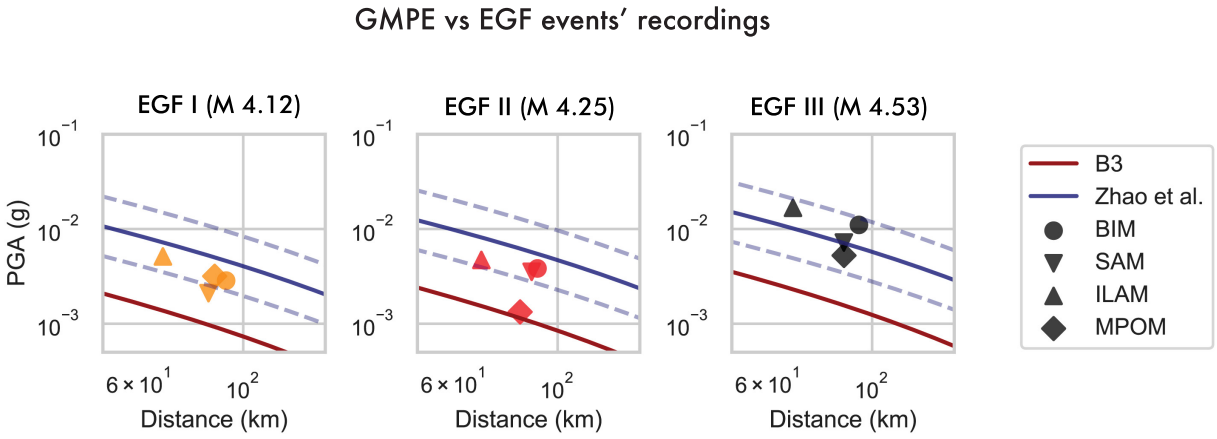

Figure 12. Comparison of recorded PGA to GMPE estimations for the three EGF events at the four Martinique stations. Zhao *et al.* (2006) model is in blue (with lower and upper limits as dashed lines), whereas the B3 model (Beauducel *et al.* 2011) is in red.

method of multi-EGF, using the RIK model, and in retrieval of the seismic catalogue of the Lesser Antilles, respectively. We also acknowledge—in chronological order—the fruitful discussions with Pascal Bernard, Luis Fabian Bonilla, Pierre-Yves Bard , Jean-Paul Ampuero, and Maria Lancieri that definitely improved the quality of this work.

We would also like to thank Gaetano Festa and the anonymous reviewer for their constructive remarks which helped improving this paper.

DATA AVAILABILITY

The seismic catalogue for Lesser Antilles used in this study is available from OVSG & OVSM (2020). Note that event `ipgp2017hushqx` is not present in the catalogue, since it has been superseded by event `ipgp2017hushqz` (see discussion in Section 3.1).

Waveform data from networks G, WI, GL and MQ (IPGP & EOST 1982; IPGP 2008c, a, b) was downloaded from the IPGP Data Center (http://datacenter.ipgp.fr).

Waveform data from networks CU and NA (Albuquerque Seismological Laboratory (ASL)/USGS 2006; KNMI 2006) was obtained through the IRIS Data Management Center (https://ds.iris.edu/ds/nodes/dmc/).

The RIKsrf code, used for modelling kinematic source rupture, is available at https://github.com/fgallovic/RIKsrf. The SourceSpec code, used to determine earthquake source parameters, is available at https://github.com/SeismicSource/sourcespec.

Data analysis has been performed using ObsPy (Krischer *et al.* 2015). Figures have been produced using the Generic Mapping Tools (Wessel *et al.* 2019) and Matplotlib (Hunter 2007).

Explanation of seaborn library tools of Python to visualise kernel density plots can be found at https://seaborn.pydata.org/tutorial/distributions.html and https://mathisonian.github.io/kde/.

REFERENCES

Aguirre, J. & Irikura, K., 1997. Nonlinearity, liquefaction, and velocity variation of soft soil layers in Port Island, Kobe, during the Hyogo-ken Nanbu earthquake, *Bull. seism. Soc. Am.,* **87**(5), 1244–1258.

Aki, K., 1967. Scaling law of seismic spectrum, *J. geophys. Res.,* **72**(4), 1217–1231.

Aki, K. & Richards, P., 2002. *Quantitative Seismology,* University Science Books.

Albuquerque Seismological Laboratory (ASL)/USGS, 2006. Caribbean USGS network, doi:10.7914/SN/CU.

Ameri, G., Gallovič, F., Pacor, F. & Emolo, A., 2009. Uncertainties in strong ground-motion prediction with finite-fault synthetic seismograms: an application to the 1984 M 5.7 Gubbio, central Italy, earthquake, *Bull. seism. Soc. Am.,* **99**(2A), 647–663.

Andrews, D., 1980. A stochastic fault model: 1. static case, *J. geophys. Res.,* **85**(B7), 3867–3877.

Anglade, A. *et al.*, 2015. Significant technical advances in broadband seismic stations in the Lesser Antilles, *Adv. Geosci.,* **40,** 43–50.

Audru, J.C., Vernier, J.L., Capdeville, B., Salindre, J.J. & Mouly, E., 2013. Preparedness actions towards seismic risk mitigation for the general public in Martinique, French Lesser Antilles: a mid-term appraisal, *Nat. Hazards Earth Syst. Sci.,* **13**(8), 2031–2039.

Barbot, S., 2020. Frictional and structural controls of seismic super-cycles at the japan trench, *Earth, Planets Space,* **72**(1), doi:10.1186/s40623-020-01185-3.

Beauducel, F., Bazin, S., Bengoubou-Valerius, M., Bouin, M.-P., Bosson, A., Anténor-Habazac, C., Clouard, V. & De Chabalier, J.-B., 2011. Empirical model for rapid macroseismic intensities prediction in Guadeloupe and Martinique, *Comptes Rendus Géoscience,* **343**(11–12), 717–728.

Bozzoni, F. *et al.*, 2011. Probabilistic seismic hazard assessment at the Eastern Caribbean Islands, *Bull. seism. Soc. Am.,* **101**(5), 2499–2521.

Brune, J.N., 1970. Tectonic stress and the spectra of seismic shear waves from earthquakes, *J. geophys. Res.,* **75**(26), 4997–5009.

Bureau de recherches géologiques et minières, 2018. Cartes géologiques imprimées des outre-mer, https://infoterre.brgm.fr.

Castro, R.R., Fabriol, H., Bour, M. & Le Brun, B., 2003. Attenuation and site effects in the region of Guadeloupe, Lesser Antilles, *Bull. seism. Soc. Am.,* **93**(2), 612–626.

Causse, M., Chaljub, E., Cotton, F., Cornou, C. & Bard, P.-Y., 2009. New approach for coupling k^{-2} and empirical Green's functions: application to the blind prediction of broad-band ground motion in the Grenoble basin, *J. geophys. Int.,* **179**(3), 1627–1644.

Causse, M., Cultrera, G., Moreau, L., Herrero, A., Schiappapietra, E. & Courboulex, F., 2017. Bayesian rupture imaging in a complex medium: The 29 May 2012 Emilia, Northern Italy, earthquake, *Geophys. Res. Lett.,* **44**(15), 7783–7792.

Courboulex, F., Converset, J., Balestra, J. & Delouis, B., 2010. Ground-motion simulations of the 2004 Mw 6.4 Les Saintes, Guadeloupe, earthquake using ten smaller events, *Bull. seism. Soc. Am.,* **100**(1), 116–130.

Davis, R.A., Lii, K.-S. & Politis, D.N., 2011. Remarks on some nonparametric estimates of a density function, in *Selected Works of Murray Rosenblatt,* pp. 95–100, Springer, doi:10.1214/aoms/1177728190.

Del Gaudio, S., Causse, M. & Festa, G., 2015. Broad-band strong motion simulations coupling k-square kinematic source models with empirical Green's functions: the 2009 L'Aquila earthquake, *J. geophys. Int.,* **203**(1), 720–736.

Del Gaudio, S., Hok, S., Festa, G., Causse, M. & Lancieri, M., 2018. Near-fault broadband ground motion simulations using empirical Green's functions: application to the Upper Rhine Graben (France–Germany) case study, in *Best Practices in Physics-based Fault Rupture Models for Seismic Hazard Assessment of Nuclear Installations,* pp. 155–177, Springer,

DeMets, C., Gordon, R.G. & Argus, D.F., 2010. Geologically current plate motions, *J. geophys. Int.,* **181**(1), 1–80.

Douglas, J., 2003. Earthquake ground motion estimation using strong-motion records: a review of equations for the estimation of peak ground acceleration and response spectral ordinates, *Earth-Sci. Rev.,* **61**(1–2), 43–104.

Douglas, J. & Mohais, R., 2009. Comparing predicted and observed ground motions from subduction earthquakes in the Lesser Antilles, *J. Seismol.,* **13**(4), 577–587.

Dujardin, A., Causse, M., Courboulex, F. & Traversa, P., 2016. Simulation of the basin effects in the Po Plain during the Emilia-Romagna seismic sequence (2012) using empirical Green's functions, *Pure appl. Geophys.,* **173**(6), 1993–2010.

Dziewonski, A.M., Chou, T.-A. & Woodhouse, J.H., 1981. Determination of earthquake source parameters from waveform data for studies of global and regional seismicity, *J. geophys. Res.,* **86**(B4), 2825–2852.

Ekström, G., Nettles, M. & Dziewoński, A., 2012. The global CMT project 2004–2010: centroid-moment tensors for 13, 017 earthquakes, *Phys. Earth planet. Inter.,* **200-201,** 1–9.

Eshelby, J.D., 1957. The determination of the elastic field of an ellipsoidal inclusion, and related problems, *Proc. R. Soc. Lond., A,* **241**(1226), 376–396.

Feuillet, N., Beauducel, F. & Tapponnier, P., 2011. Tectonic context of moderate to large historical earthquakes in the Lesser Antilles and mechanical coupling with volcanoes, *J. geophys. Res.: Solid Earth,* **116**(B10), doi:10.1029/2011JB008443.

Frankel, A., 1991. High-frequency spectral falloff of earthquakes, fractal dimension of complex rupture, b value, and the scaling of strength on faults, *J. geophys. Res.,* **96**(B4), 6291–6302.

Gallovič, F., 2016. Modeling velocity recordings of the Mw 6.0 South Napa, California, earthquake: Unilateral event with weak high-frequency directivity, *Seismol. Res. Lett.,* **87**(1), 2–14.

Ghofrani, H., Atkinson, G.M. & Goda, K., 2013. Implications of the 2011 M9.0 Tohoku Japan earthquake for the treatment of site effects in large earthquakes, *Bull. Earthq. Eng.,* **11**(1), 171–203.

Hartzell, S., Leeds, A., Frankel, A., Williams, R.A., Odum, J., Stephenson, W. & Silva, W., 2002. Simulation of broadband ground motion including nonlinear soil effects for a magnitude 6.5 earthquake on the Seattle fault, Seattle, Washington, *Bull. seism. Soc. Am.,* **92**(2), 831–853.

Hartzell, S.H., 1978. Earthquake aftershocks as Green's functions, *Geophys. Res. Lett.,* **5**(1), 1–4.

Hunter, J.D., 2007. Matplotlib: a 2D graphics environment, *Comput. Sci. Eng.,* **9**(3), 90–95.

Hutchings, L. & Viegas, G., 2012. Application of empirical green's functions in earthquake source, wave propagation and strong ground motion studies, *Earthq. Res. Anal.-New Front. Seismol.,* 87–140. Available at: https://www.intechopen.com/books/earthquake-research-and-analysis-new-frontiers-in-seismology/application-of-empirical-green-s-functions-in-earthquake-source-wave-propagation-and-strong-ground-m.

Hutchings, L., Ioannidou, E., Foxall, W., Voulgaris, N., Savy, J., Kalogeras, I., Scognamiglio, L. & Stavrakakis, G., 2007. A physically based strong ground-motion prediction methodology; application to PSHA and the 1999 $M_w = 6.0$ Athens earthquake, *J. geophys. Int.,* **168**(2), 659–680.

Imperatori, W. & Mai, P.M., 2012. Sensitivity of broad-band ground-motion simulations to earthquake source and Earth structure variations: an application to the Messina Straits (Italy), *J. geophys. Int.,* **188**(3), 1103–1116.

IPGP, 2008a. Data collection of the seismological and volcanological observatory of Guadeloupe, Institut de physique du globe de Paris (IPGP). Available at: https://doi.org/10.18715/GUADELOUPE.OVSG.

IPGP, 2008b. Data collection of the seismological and volcanological observatory of Martinique, Institut de physique du globe de Paris (IPGP). Available at: https://doi.org/10.18715/MARTINIQUE.OVSM.

IPGP, 2008c. GNSS, seismic broadband and strong motion permanent networks in West Indies, Institut de physique du globe de Paris (IPGP), Université de Paris. Available at: https://doi.org/10.18715/ANTILLES.WI

IPGP, EOST, 1982. GEOSCOPE - French Global Network of broadband seismic stations, Institut de Physique du Globe de Paris & Ecole et Observatoire des Sciences de la Terre de Strasbourg (EOST), doi:10.18715/GEOSCOPE.G.

Irikura, K., 1986. Prediction of strong acceleration motion using empirical Green's function, in *Proceedings of the 7th Japan Earthquake Engineering Symposium,* Vol. **151,** pp. 151–156, Available at: http://www.kojiro-irikura.jp/pdf/7th_J_Earthquake_Eng_Sympo.pdf.

Kamae, K. & Irikura, K., 1998. Source model of the 1995 Hyogo-ken Nanbu earthquake and simulation of near-source ground motion, *Bull. seism. Soc. Am.,* **88**(2), 400–412.

KNMI, 2006. Caribbean Netherlands Seismic Network, Royal Netherlands Meteorological Institute (KNMI). Other/Seismic Network. Available at: https://10.21944/dffa7a3f-7e3a-3b33-a436-516a01b6af3f.

Kotha, S.R., 2018. Quantification of uncertainties in seismic ground-motion prediction, *PhD thesis*, Universität Potsdam Potsdam, http://nbn-resolving.de/urn/resolver.pl?urn=urn:nbn:de:kobv:517-opus4-415743.

Krischer, L., Megies, T., Barsch, R., Beyreuther, M., Lecocq, T., Caudron, C. & Wassermann, J., 2015. ObsPy: a bridge for seismology into the scientific Python ecosystem, *Computat. Sci. Discov.,* **8**(1), 014003.

Laigle, M. *et al.*, 2013. Seismic structure and activity of the north-central Lesser Antilles subduction zone from an integrated approach: similarities with the Tohoku forearc, *Tectonophysics,* **603,** 1–20.

Lancieri, M., Renault, M., Berge-Thierry, C., Gueguen, P., Baumont, D. & Perrault, M., 2015. Strategy for the selection of input ground motion for inelastic structural response analysis based on naïve Bayesian classifier, *Bull. Earthq. Eng.,* **13**(9), 2517–2546.

Madariaga, R. & Ruiz, S., 2016. Earthquake dynamics on circular faults: a review 1970–2015, *J. Seismol.,* **20**(4), 1235–1252.

McGuire, J. & Ben-Zion, Y., 2017. Detailed analysis of earthquake directivity in the San Jacinto Fault Zone, SCEC Final Report, Project 16104, https://www.scec.org/proposal/report/16104.

Oral, E., Gélis, C. & Bonilla, L.F., 2019. 2-D P-SV and SH spectral element modelling of seismic wave propagation in non-linear media with pore-pressure effects, *J. geophys. Int.,* **217**(2), 1353–1365.

OVSG, OVSM, 2020. Unified seismic catalogue for the Lesser Antilles, 2014–2019. Available at: http://doi.org/10.18715/IPGP.2020.kgmbivor.

Pacor, F., Ameri, G., Gallovic, F. & D'Amico, M., 2017. Ground motion variability from finite fault simulations, in *Proceedings of the 16th World Conference on Earthquake (16WCEE),* Santiago, Chile, 9–13.

Parzen, E., 1962. On estimation of a probability density function and model, *Ann. Math. Stat.,* **33**(3), 1065–1076.

Paulatto, M., Laigle, M., Galve, A., Charvis, P., Sapin, M., Bayrakci, G., Evain, M. & Kopp, H., 2017. Dehydration of subducting slow-spread oceanic lithosphere in the Lesser Antilles, *Nat. Commun.,* **8,** 15980.

Pavic, R., Koller, M.G., Bard, P.-Y. & Lacave-Lachet, C., 2000. Ground motion prediction with the empirical Green's function technique: an assessment of uncertainties and confidence level, *J. Seismol.,* **4**(1), 59–77.

Pulido, N., Ojeda, A., Atakan, K. & Kubo, T., 2004. Strong ground motion estimation in the Sea of Marmara region (Turkey) based on a scenario earthquake, *Tectonophysics,* **391**(1–4), 357–374.

Ragon, T., Sladen, A. & Simons, M., 2019. Accounting for uncertain fault geometry in earthquake source inversions–II: application to the M_w 6.2 Amatrice earthquake, central Italy, *J. geophys. Int.,* **218**(1), 689–707.

Régnier, J., Cadet, H., Bonilla, L.F., Bertrand, E. & Semblat, J.-F., 2013. Assessing nonlinear behavior of soils in seismic site response: Statistical analysis on KiK-net strong-motion data, *Bull. seism. Soc. Am.,* **103**(3), 1750–1770.

Ripperger, J., Mai, P. & Ampuero, J.-P., 2008. Variability of near-field ground motion from dynamic earthquake rupture simulations, *Bull. seism. Soc. Am.,* **98**(3), 1207–1228.

Ruiz, J., Baumont, D., Bernard, P. & Berge-Thierry, C., 2011. Modelling directivity of strong ground motion with a fractal, k^{-2}, kinematic source model, *J. geophys. Int.,* **186**(1), 226–244.

Ruiz, M. *et al.*, 2013. Seismic activity offshore Martinique and Dominica islands (Central Lesser Antilles subduction zone) from temporary onshore and offshore seismic networks, *Tectonophysics,* **603,** 68–78.

Russo, R.M., Okal, E.A. & Rowley, K.C., 1992. Historical seismicity of the southeastern Caribbean and tectonic implications, *Pure appl. Geophys.,* **139**(1), 87–120.

Satriano, C., 2021. SourceSpec – Earthquake source parameters from S-wave displacement spectra, Available at: http://doi.org/10.5281/zenodo.4779492.

Satriano, C., Dionicio, V., Miyake, H., Uchida, N., Vilotte, J.-P. & Bernard, P., 2014. Structural and thermal control of seismic activity and megathrust rupture dynamics in subduction zones: Lessons from the Mw 9.0, 2011 Tohoku earthquake, *Earth planet. Sci. Lett.,* **403,** 287–298.

Sørensen, M.B., Pulido, N. & Atakan, K., 2007. Sensitivity of ground-motion simulations to earthquake source parameters: a case study for Istanbul, Turkey, *Bull. seism. Soc. Am.,* **97**(3), 881–900.

Spudich, P., Cirella, A., Scognamiglio, L. & Tinti, E., 2019. Variability in synthetic earthquake ground motions caused by source variability and errors in wave propagation models, *J. geophys. Int.,* **219**(1), 346–372.

Vallée, M., Charléty, J., Ferreira, A.M., Delouis, B. & Vergoz, J., 2011. SCARDEC: a new technique for the rapid determination of seismic moment magnitude, focal mechanism and source time functions for large earthquakes using body-wave deconvolution, *J. geophys. Int.,* **184**(1), 338–358.

Wang, H., Igel, H., Gallovič, F. & Cochard, A., 2009. Source and basin effects on rotational ground motions: comparison with translations, *Bull. seism. Soc. Am.,* **99**(2B), 1162–1173.

Weil-Accardo, J. *et al.*, 2016. Two hundred thirty years of relative sea level changes due to climate and megathrust tectonics recorded in coral microatolls of Martinique (French West Indies), *J. geophys. Res.,* **121**(4), 2873–2903.

Wessel, P., Luis, J.F., Uieda, L., Scharroo, R., Wobbe, F., Smith, W.H.F. & Tian, D., 2019. The Generic Mapping Tools Version 6, *Geochem. Geophys. Geosyst.,* **20**(11), 5556–5564.

Withers, K.B., Olsen, K.B., Shi, Z. & Day, S.M., 2019. Validation of deterministic broadband ground motion and variability from dynamic rupture simulations of buried thrust earthquakes validation of deterministic broadband ground motion and variability, *Bull. seism. Soc. Am.,* **109**(1), 212–228.

Zhao, J.X. *et al.*, 2006. Attenuation relations of strong ground motion in Japan using site classification based on predominant period, *Bull. seism. Soc. Am.,* **96**(3), 898–913.

SUPPORTING INFORMATION

Supplementary data are available at *GJI* online.

Table S1. *P*-wave velocity and rock density profile for the studied zone (provided by personal communication of Prof Alexandre Narcessian).

Figure S1. Example of the partition of fault plane for the selected EGFs in multi-EGF approach. EGF hypocentres are shown by dots.

Figure S2. Spectral ratio between the synthetic ground motion and the reference EGF I at east–west component of station BIM (apparent source–time function spectrum). Compared to fig. 4(a) of Causse *et al.* (2009), we do not see high-frequency amplification of the spectral level, due to EGF summation, and the apparent spectrum retains an 'omega-square' falloff. Here we considered the most directive case where the hypocentre is set at fault top, and the rupture is towards the island.

Figure S3. Change of peak ground acceleration by the choice of pulse width in the case of a fault with high aspect ratio. Pulse width is in unit of fault width.

Figure S4. ISOLA solution for the EGF II event. (a) Stations used in the ISOLA. (b) Best solution of depth and focal mechanism. (c) Comparison of inverted seismograms and synthetic solution.

Figure S5. Verification of the reverse faulting by the direction of first vertical pulse for the three EGF events. Stations that recorded downward motion are shown in red. Star denotes event epicentre; noisy stations are shown in gray.

Figure S6. Corrected EGF signals. Velocity-time histories for each channel of EGF I at station BIM.

Figure S7. Same as Fig. S6 for EGF II.

Figure S8. Same as Fig. S6 for EGF III.

Figure S9. Same as Fig. S6 for station ILAM and EGF I.

Figure S10. Same as Fig. S6 for station ILAM and EGF II.
Figure S11. Same as Fig. S6 for station ILAM and EGF III.
Figure S12. Same as Fig. S6 for station MPOM and EGF I.
Figure S13. Same as Fig. S6 for station MPOM and EGF II.
Figure S14. Same as Fig. S6 for station MPOM and EGF III.
Figure S15. Same as Fig. S6 for station SAM and EGF I.
Figure S16. Same as Fig. S6 for station SAM and EGF II.
Figure S17. Same as Fig. S6 for station SAM and EGF III.
Figure S18. Same as Fig. 6 for station BIM.
Figure S19. Same as Fig. 6 for station SAM.
Figure S20. Same as Fig. 6 for station MPOM.
Figure S21. STF on fault plane shown for cluster A case (top row), and cluster B case (bottom row). The zoomed window for 3 km is shown for each case in the second column.
Figure S22. Comparison of cluster A (in blue) and B (in red) of synthetic ground motion with GMPE curves (in grey) by peak ground acceleration. Mean GMPE curves are shown in solid lines; the lower and upper limits of GMPE curves are shown in dashed lines. Each diagram stands for the analysis of a station: BIM, SAM, ILAM and MPOM. We used soil class #4 for GMPEs.
Figure S23. Same as Fig. 9 for use of soil class #1 (rock).
Figure S24. Same as Fig. S22 for use of soil class #1 (rock).
Figure S25. Same as Fig. 9 when signals are LP filtered at 4.57 Hz. We used soil class #4 for GMPEs. We removed the spectral acceleration plots of 5 Hz.
Figure S26. Same as Fig. S1 when EGF II is updated after the new catalogue data.
Figure S27. Same as Fig. 7 when EGF II is updated after the new catalogue data.